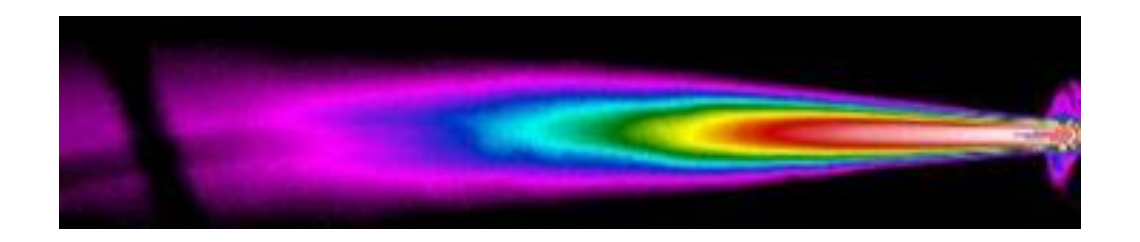
THESIS FOR THE DEGREE OF LICENTIATE OF ENGINEERING

Experimental studies of heat transfer in cement rotary kilns and CO₂ plasma jets designed for future electrification

Ibrahim Qasim



Department of Space, Earth, and Environment
CHALMERS UNIVERSITY OF TECHNOLOGY

Gothenburg, Sweden 2025

Experimental studies of heat transfer in cement rotary kilns and CO ₂ plasma jets designed for future electrification							
Ibrahim Qasim							
© Ibrahim Qasim, 2025.							
Department of Space, Earth, and Environment							
Chalmers University of Technology							
SE-412 96 Gothenburg							
Sweden							
Printed by Chalmers Reproservice							
Gothenburg, Sweden 2025							

Experimental studies of heat transfer in cement rotary kilns and CO₂ plasma jets designed for future electrification

Ibrahim Qasim

Division of Energy Technology

Department of Space, Earth, and Environment

Chalmers University of Technology

Abstract

Fossil fuel combustion remains the dominant source of heat in energy-intensive industries such as cement and glass manufacturing, contributing significantly to CO₂ and particulate emissions. To meet decarbonization goals, electrification of thermal processes, including thermal plasma and hydrogen combustion, is gaining momentum, as well as heating resistance elements for some applications. Experimental studies are needed to understand the heat transfer mechanisms, support model validation, and guide process adaptation for the implementation of electrification.

This thesis studies the heat transfer, energy efficiency, and radiative characteristics of rotary kilns during propane combustion and oxygen-enriched propane combustion, as well as the resistance heating elements that contribute to the development of low-emissions industrial systems. The work is based on three experimental studies.

In **Paper I**, three heating techniques for rotary kiln with distinct thermal signatures are investigated. Resistance heating produces a uniform axial temperature profile, reducing thermal gradients and minimizing flue gas losses. Oxygen-enriched combustion yields the lowest flue gas losses among the combustion cases and is the only method to achieve the high temperatures required for clinker formation. When these cases are scaled to industrial conditions using a validated heat balance methodology, the combustion systems benefited from reduced surface heat losses due to lower surface-to-volume ratios, while resistance heating retains its advantage of low flue gas losses through improved thermal control.

Paper II demonstrates that using crushed cement raw meal as the bed material facilitates the formation of a coating layer on the inner kiln wall. This layer acts as a thermal insulator, reducing surface heat losses and stabilizing the inner wall temperatures.

Paper III provides experimental insight into CO₂ plasma jets by mapping the axial radiative intensity profile under different arc currents and gas flows. A sharp radiative peak is observed near the burner outlet, followed by a rapid decline and stabilization downstream. This behavior highlights the transition from localized radiative emission to convective transport along the jet, offering valuable data for future modeling and integration of plasma torches into rotary kilns.

Keywords: Radiative heat transfer, rotary kilns, coating layer, thermal plasma

List of Publications

The thesis is based on the following papers, which are referred to in the text according to their Roman numerals:

- I. Qasim, I.; Gunnarsson, A.; Normann, F.; Wilhelmsson, B.; Zether, A.; Andersson, K. Heat Loss Quantification and Heat Transfer in Rotary Kilns for Calcination and Clinker Formation: From Combustion and Electrification at 150 kW to Industrial Scale. Ind Eng Chem Res 2025, 64 (23), 11531–11543.
- II. Qasim, I.; Gunnarsson, A.; Normann, F.; Wilhelmsson, B.; Zether, A.; Andersson, K. Temperature conditions in a 150-kW pilot rotary kiln: Impact of bed material. Clearwater Clean Energy Conference, Florida, U.S.A, 2024.
- III. Qasim, I.; Mishra, S; Gunnarsson, A.; Normann, F.; Andersson, K. Radiative characteristics and heat transfer regime transitions in CO2-based thermal plasma jets (Submitted to Experimental Thermal and Fluid Science Journal).

Author's contribution

Ibrahim Qasim is the main author of Papers I, II, and III, responsible for the execution of the experiments, data analysis, and the writing of the manuscripts. Assistant Professor Adrian Gunnarsson contributed to the experimental design, measurement evaluation, and energy balance calculations across all the papers. Dr. Bodil Wilhelmsson and Alexander Zether supported the experimental work described in Papers I and II. Dr. Saumitra Mishra and Assistant Professor Adrian Gunnarsson contributed to the experimental measurements and radiative and data analyses in Paper III. Professor Fredrik Normann and Professor Klas Andersson provided guidance throughout the work and contributed to discussions, writing, and editing of all three papers.

Acknowledgments

First and foremost, I would like to express my sincere gratitude to my supervisor, Fredrik Normann, my examiner, Klas Andersson, and my co-supervisor, Adrian Gunnarsson. Fredrik, your critical feedback and sharp eye for clarity have been invaluable. You taught me how to think like a researcher and how to communicate with purpose. Klas, thank you for your constant encouragement and for giving me the freedom to explore ideas, while still making sure that I stayed on track. And Adrian, thank you for your endless patience and guidance; I'm fairly certain no one else has endured as many door knocks from me as you have. You've always been there to discuss, double-check, and remind me not to burn myself out.

As the experimentalist in the group, I owe huge thanks to everyone who made the measurements possible. At KC, thank you to Thomas Allgurén, Johannes Öhlin, and Rustan Hvitt for your technical expertise and steady support. Heidelberg Materials and the Swedish Energy Agency are acknowledged for the financial support for this work. At Heidelberg Materials, I am grateful to Alexander Zether and Bodil Wilhelmsson for their excellent collaboration and valuable inputs as co-authors. Working together with you has been both rewarding and fun.

To my colleagues and friends at the High Temperature Group, thank you for the discussions, ideas, and humor that made every project better. Saumitra, Elias, Alice, Rosa, Javier, and Samuel, thank you for the countless kiln talks, data debates, and shared motivation (yes, we still love kilns). A special thanks to Saumitra: you've been the perfect partner in experiments and "jugaads", always finding a creative fix when things didn't go as planned.

A heartfelt thanks to my office mate, Nauman Saeed: thank you for making sure that I never felt lonely and for constantly pushing me to take breaks and get out of the office. Your hospitality over the last three years, the endless cups of chai over cricket matches, and the delicious desi food made it feel like home away from home.

To my family, thank you for your love, prayers, and belief in me, even when I decided to move halfway across the world. To my friends, both in Pakistan and across Europe, thank you for the laughter, adventures, and reminders that life exists beyond experiments.

Finally, to my amazing wife, Ayesha: thank you for your endless support, patience, and love through all the ups and downs. You've been my calm in the storm, my editor, and my biggest source of strength. The last few years have been intense, but we've faced it all together, and as we always say, *this too shall pass*. I'm excited for what lies ahead, both in research and in life, and I couldn't imagine continuing this journey without you by my side.

Ibrahim Qasim

Gothenburg, Sweden, 2025

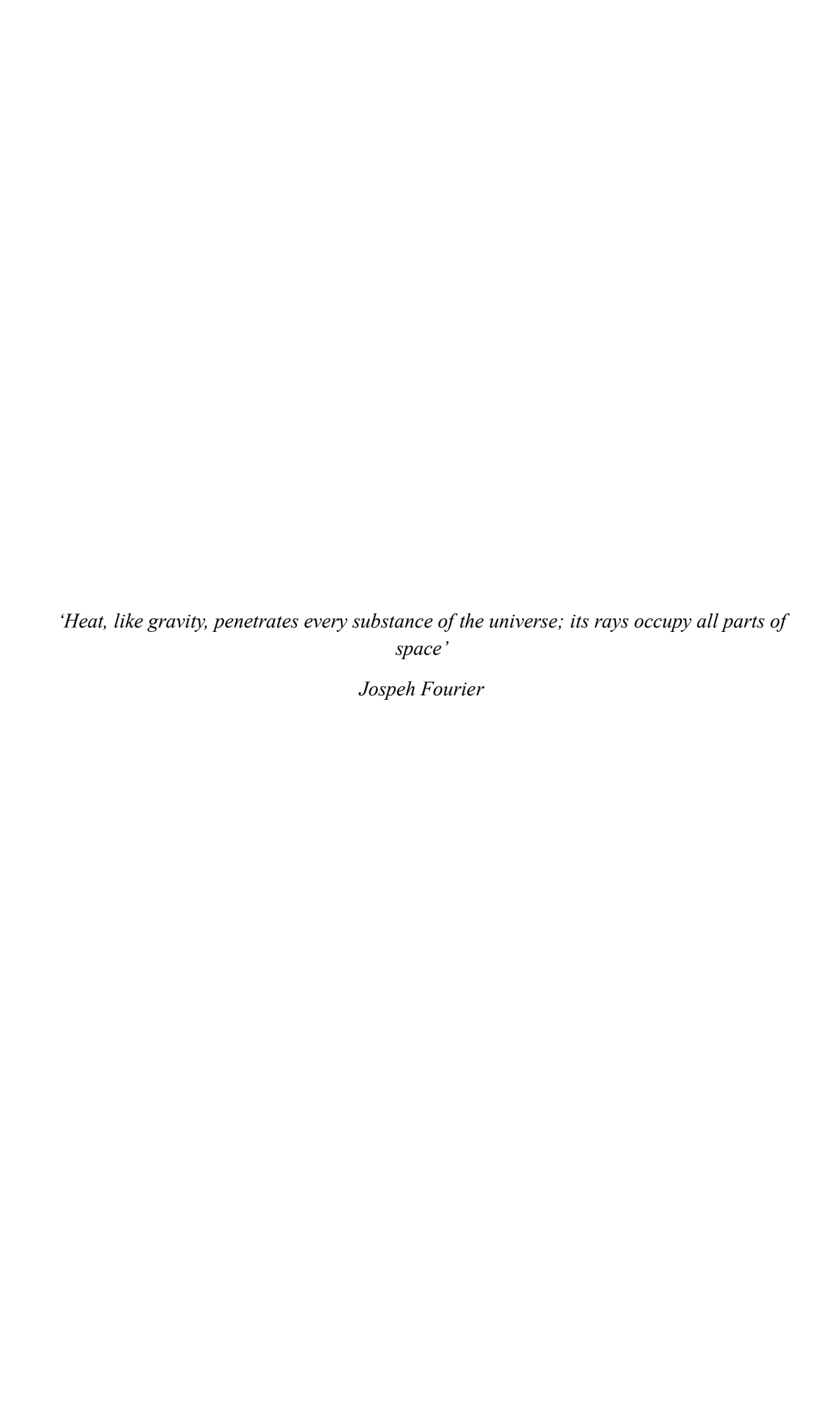
Outline

This licentiate thesis consists of a summary of the work and three appended papers. The summary is organized into six chapters that collectively address heat transfer mechanisms and electrification strategies for rotary kilns in cement production.

Chapters 1 and 2 introduce the motivation for this research, review previous studies on high-temperature process electrification, and present the background theory of heat transfer and radiation in rotary kilns. Chapter 3 describes the experimental setups and measurement methods used in the pilot-scale rotary kiln and in the open-air CO₂-based plasma experiments, including the instrumentation used for the temperature, radiative intensity, and energy balance analyses. Chapter 4 presents and discusses the results from the three appended papers. Paper I investigates the heat transfer and energy losses in a 150-kW rotary kiln operated with propane combustion, oxygen-enriched combustion, and resistance heating, including an analysis of scaling to industrial conditions. Paper II examines the effect of the bed material on wall heat losses through coating layer formation and its influence on the thermal behavior of the kiln. Paper III characterizes the radiative characteristics and heat transfer regime transitions in CO₂-based thermal plasma jets, in order to evaluate their suitability as a heat source for the kiln. Chapters 5 and 6 summarize the main conclusions drawn from the studies and suggest directions for future work, including plasma integration into the pilot kiln and the development of diagnostic and modeling tools for emissivity and temperature estimations.

Table of Contents

1.	Intro	oduction	1			
	1.1	Scope and Aim	2			
2.	Back	ground	5			
	2.1	Rotary kiln in high temperature industrial processes	5			
	2.2	Rotary kilns in cement manufacturing	6			
	2.3	Rotary kiln- heat transfer mechanism	6			
	2.4	Thermal plasma	12			
3.	Meth	nod	19			
	3.1	Experimental setup of Kiln Zero	20			
	3.2	Experimental setup of DC non-transferred CO ₂ plasma system	22			
	3.3	Measurement Techniques	23			
	3.3.1	Narrow Angle Radiometer (NAR)	23			
	3.3.2	Ellipsoidal radiometer	24			
	3.3.3	InfraRed thermography (IR)	24			
	3.3.4	Fourier-Transform Infrared Spectroscopy (FTIR)	25			
	3.4	Measurement method and operational parameters	25			
	3.5	Mass and energy balance methodology	28			
	3.1	Estimation of the thickness of the coating layer	30			
4.	Selec	cted Results and Discussion	33			
	4.1	Experimental studies in Kiln Zero	33			
	4.2	Experimental studies in the open air	40			
5.	Conc	clusion	45			
6.	Future Work47					
R	eference	es	49			



1. Introduction

Growing concerns regarding climate change and the levels of industrial carbon emissions have imposed considerable pressure on energy-intensive sectors to transition towards sustainable production routes. Cement production is one of the most-emissions-intensive industrial processes globally, contributing approximately 8% of all CO₂ emissions. These emissions originate from both the calcination of limestone and the combustion of fossil fuels, the latter of which is required to achieve the high process temperatures (>1,400°C) necessary for clinker formation. The clinker production process is typically fueled by coal and natural gas, although increasingly also by alternative fuels such as used tires, industrial residues, and waste-derived materials (collectively referred to as "fluff"), making it a significant contributor to industrial greenhouse gas emissions.

The manufacture of Portland cement involves a series of thermochemical stages. Among these, calcination in the preheater and calciner is the most energy-demanding step, while clinker formation in the rotary kiln requires the highest process temperatures. The latter stage occurs in a rotary kiln, which is a refractory-lined, rotating reactor that converts raw meal into clinker at high temperatures. Although rotary kilns offer robust operation and continuous throughput, they suffer from substantial thermal inefficiencies, including the loss of sensible heat in the exhaust gas streams of the kiln system, radiative heat losses from the shell, and air leakage. These factors, combined with the continued use of carbon-intensive fuels, underscore the need for alternative, high-efficiency heating solutions.

For energy-intensive industries industry, electrification is emerging as a central pathway to reduce reliance on fossil fuels and lower greenhouse gas emissions. For cement production, this transition requires heating solutions that can replicate the extreme temperatures and heat fluxes of conventional fuel combustion, while maintaining process stability and product quality. In Sweden, Heidelberg Materials Cement Sweden AB, one of the largest global cement manufacturers, has committed to achieving net-zero carbon emissions across its operations by Year 2030¹. To support this transition, the company has initiated major innovation programs, including the CemZero project², which is focused on investigating fully electrified alternatives to fossil-based heating in cement kilns. Within this framework, thermal plasma systems have been identified as a promising option owing to their potential to deliver combustion-free, high-temperature heat using renewable electricity.

Thermal plasmas, especially those generated using CO₂ as the working gas, can produce extremely high energy densities and radiative fluxes without direct fuel combustion. When powered by renewable electricity, CO₂-based plasma systems provide a closed-loop, combustion-free heating source with minimal direct generation of CO₂. CO₂-based plasma systems emit intense infrared radiation, with spectral peaks that overlap significantly with the main absorption bands of CO₂ (particularly around 4–5 µm and 15 µm). This overlap enhances the radiative heat transfer in CO₂-rich environments, making

such systems particularly relevant for high-temperature industrial processes. However, integrating plasma jets into rotary kiln systems raises new challenges in relation to heat transfer distribution, the shift in mode of heat transfer, energy efficiency, and process control.

This thesis is concerned with both conventional and emerging kiln-heating technologies, focusing on the transition from combustion-based processes to electrified high-temperature processes. This thesis first evaluates the heat transfer and energy losses in a 150-kW pilot rotary kiln operated with propane, oxygen-enriched combustion, and electrical resistance heating. These measurements establish a thermal performance baseline under industrially relevant conditions. The radiative behavior of CO₂-based thermal plasma is experimentally studied in open air at powers up to 300-kW_{el}, to characterize its standalone heat transfer performance before integration into the kiln. This allows for the evaluation of plasma-specific radiative properties under controlled conditions. The combined results support the potential integration of plasma heating into rotary kiln systems for purpose of low-carbon cement production. In addition to its relevance to cement production, the knowledge generated here on plasma heat transfer and radiative efficiency is transferable to other sectors that are seeking electrified, high-intensity thermal processing solutions.

1.1 Scope and Aim

The overall aim of this thesis is to determine how different heating technologies – conventional combustion, electrical resistance, and CO₂-based thermal plasma – influence the heat transfer, energy efficiency, and suitability for integration of thermal heating into the rotary kilns used in cement production. The motivation lies in reducing the cement industry's reliance on fossil fuels, thereby lowering CO₂ emissions while still achieving the extreme temperatures and stable operating conditions required for clinker formation. The present work contributes to the field by experimentally characterizing the heat transfer behaviors and scalability of alternative heating systems under realistic process conditions.

To achieve this overarching aim, the work addresses the following Research Questions:

- RQ1 How do different heating technologies affect the overall heat transfer and energy balance in pilot rotary kilns?
- RQ2 How do different bed materials influence wall heat losses in rotary kilns related to coating layer formation?
- RQ3 How do different heating technologies scale to industrial rotary kilns?
- RQ4 Which of the radiative characteristics and heat transfer regime transitions of CO₂-based thermal plasma jets are relevant to kiln heating?

The research follows a stepwise approach to answer these questions:

- Step 1 (RQ1 and RQ2): Experimental assessment of heat transfer and energy losses in a 150-kW pilot rotary kiln operated with propane combustion, oxygen-enriched combustion, and electrical resistance heating elements with two main types of bed material, limestone and mealed limestone with additives, referred to as raw meal. The study includes determining detailed temperature profiles, radiative and convective loss estimation, and closing the mass and energy balances. In relation to RQ2, particular attention is given to the effect of coating formation observed with raw meal, whereas no such coating was formed with limestone. with the raw meal. The detailed study of the heat transfer conditions within the kiln will act as a reference for future studies in which heat will be supplied by thermal plasma. (*Paper I and Paper II*)
- Step 2 (RQ3): Scaling the energy balance results to industrial rotary kilns, quantifying the impacts of heating technologies and kiln dimensions on flue gas losses, surface radiation, and overall energy efficiency. (*Paper I*)
- Step 3 (RQ4): Experimental characterization of CO₂-based thermal plasma in open air at powers up to 300 kW_{el}, focusing on the radiative intensity distribution and the relative contributions of radiation and convection to spatial heat transfer, behavior, so as to evaluate the suitability of thermal plasma as a combustion-free heat source for high-temperature processes. (*Paper III*)

In addition, future work aims to develop measurement technologies to evaluate the local thermal plasma temperature conditions and to estimate the emissivity of the plasma plume.

The results from Steps 1 and 2 are presented in Papers I and II, while Step 3 is addressed in Paper III. Future work will build on these findings to support the integration of plasma systems into a pilot and full-scale rotary kiln.

2. Background

2.1 Rotary kiln in high temperature industrial processes

The rotary kiln is a critical component in numerous high-temperature industrial processes, most notably in cement manufacturing, iron ore pelletization, pulp and paper production, and lime production (see references^{3–6}). Since its invention by Frederick Ransome in 1885 for the cement industry, the rotary kiln has evolved into a robust and versatile thermal reactor that is capable of processing a wide variety of solid materials through intense heat treatment⁷. A rotary kiln consists of a long, cylindrical, slightly inclined shell that rotates slowly about its axis. The raw material is introduced at the upper end and moves progressively towards the lower, hotter end due to the combined effects of gravity and kiln rotation. Heat is supplied either directly via combustion within the kiln (direct-fired kilns) or indirectly via external sources (indirect-fired kilns), depending on the thermal requirements of the process. The present work focuses on direct-fired rotary kilns (Figure 1), which are commonly used in many industrial processes. In these systems, the burner is positioned at the lower end of the kiln, where the fuel is combusted to generate a high-temperature flame.

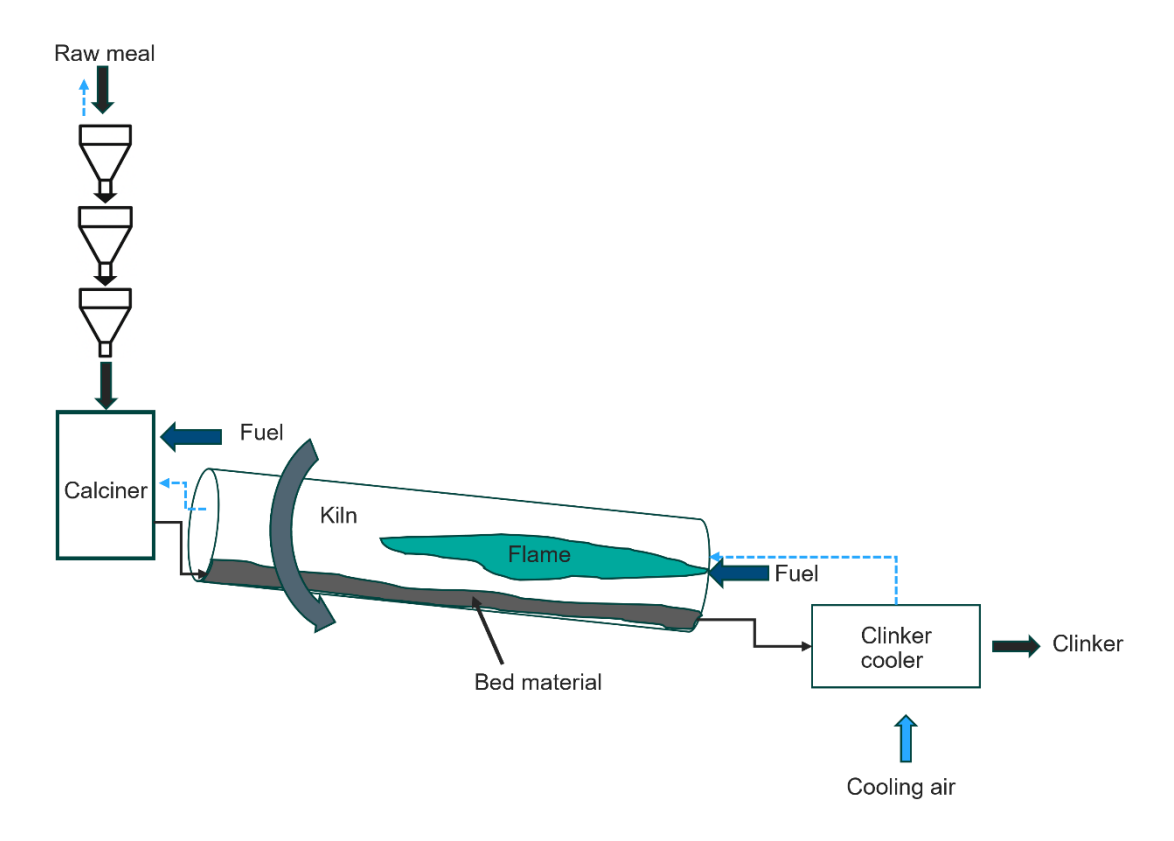


Figure 1 Simplified schematic of a direct-fired rotary kiln used for cement production.

Some of the major challenges associated with large industrial rotary kilns are their high levels of energy consumption and substantial CO₂ emissions resulting from fossil fuel combustion. The choice of fuel is primarily driven by its calorific value, cost, availability, and combustion characteristics⁸. Coal remains

a commonly used fuel due to its high calorific value and ability to reach high temperatures readily, although propane, natural gas, and fuel mixtures are also used depending on site-specific constraints.

2.2 Rotary kilns in cement manufacturing

Among the many applications of rotary kilns, cement manufacturing presents a particularly energyintensive process in which the kiln plays a central role in transforming the raw meal into clinker. In cement plants, this transformation involves several thermochemical stages that are tightly integrated to ensure efficiency. The process begins with the preheater tower, where raw meal passes through a series of cyclones and is gradually heated by rising hot gases from the kiln and calciner. This preheating stage improves thermal efficiency by recovering heat from the kiln exhaust gases. The preheated meal then enters the calciner which is a separate vessel located before the kiln, where the main part of it undergoes calcination at around 850°-900°C. Here, limestone (CaCO₃) decomposes into lime (CaO) and releases CO₂. The use of the calciner allows part of the fuel to be burned outside the rotary kiln, thereby improving temperature control and enabling higher production rates. The partially calcined material then enters the rotary kiln, where the second thermal transformation, clinkerization, occurs. At temperatures of up to 1450°C, the lime reacts with silica, alumina, and iron oxides to form clinker minerals such as alite (C₃S) and belite (C₂S)⁹. The clinker-forming reactions require sustained hightemperature input to proceed, building on the strongly endothermic calcination step. This heat demand has historically been met by fossil fuel combustion. As the kiln rotates, material near the wall is lifted and cascades back down, promoting uniform exposure to the heat source and facilitating efficient heat transfer. However, this recirculating motion, combined with local variations in temperature and chemical composition, can also lead to the formation of boulders and rings along the kiln wall, which may cause severe disruption and even force shutdowns of the cement production process. After exiting the kiln, the hot clinker enters the clinker cooler, where it is rapidly quenched with ambient or preheated air. This step recovers thermal energy and reduces the temperature of the clinker for safe handling. The recovered heat is often reused as secondary air for combustion in the kiln or calciner, contributing to the plant's overall energy efficiency. Despite their efficiency, rotary kilns are energy-intensive and contribute significantly to industrial CO₂ emissions. In cement production, roughly 60% of the CO₂ emissions originate from the calcination reaction itself, while the remaining 40% are fuel-related¹⁰. Given the critical role of the kiln in the cement manufacturing process and its substantial carbon footprint, it has become a primary target in global efforts to decarbonize the cement industry.

2.3 Rotary kiln- heat transfer mechanism

The thermal performances of rotary kilns are governed by a complex interplay of heat transfer modes, conduction, convection, and radiation occurring between the hot gas phase, the rotating kiln wall, and the granular bed of solids. The relative contribution of each mode varies with location along the kiln,

operating conditions, and fuel type, although in high-temperature cement kilns, radiation is typically the dominant heat transfer mechanism, particularly in the flame zone near the burner¹¹.

Conduction occurs both through particle–particle contact within the bed and from the hot refractory wall to the bed material when they are in contact. The latter becomes more relevant in zones with low gas velocities or in packed-bed conditions close to the inlet. Convection arises due to the motion of combustion gases over the solid bed and internal surfaces. The gas-solid convective heat transfer coefficients are influenced by the gas velocity, as well as by the internal geometry and rotation of the kiln¹² and has been shown to affect significantly the temperature distribution in rotary kilns¹³. In cement kilns, chain sections are often installed near the feed inlet to enhance convective heat transfer by increasing gas—solid contact and recovering waste heat from the exhaust gases⁷.

Radiation, particularly thermal radiation from the luminous flame, hot gas, and high-temperature wall products, plays a dominant role in heat transfer in the burning zone, where clinker formation occurs⁷. The contribution of radiation increases sharply with temperature, as described by the Stefan–Boltzmann law, and it becomes the primary mode of energy exchange between the flame, gas, wall, and bed. Radiative heat transfer is a function of the emissivity and temperature of the flame, wall, and bed. In direct-fired cement kilns, the radiative environment is further enriched by particulate radiation from soot and ash, particularly during coal or solid fuel combustion. These particles emit and absorb radiation, significantly enhancing the overall radiative heat transfer to the solids and refractory lining^{11,14}.

Towards understanding the heat transfer conditions and losses in rotary kilns, numerous studies have investigated the heat transfer mechanisms of convection, conduction, and radiation across a range of operating conditions and kiln scales. Early experimental work, such as that carried out by Tscheng and Watkinson ¹², focused on pilot-scale rotary kilns and explored how parameters such as rotational speed, gas flow rate, and fill level affect convective heat transfer to the wall and bed. These studies established empirical correlations between gas-solid and gas-wall convective coefficients and operational parameters, establishing a basis for one-dimensional (1-D) thermal models of rotary kilns. Similarly, Gorog et al. ¹⁵ expanded the understanding of convective transfer by incorporating secondary air effects and regenerative wall behavior. These studies have provided insights and have been widely used to inform thermal models. However, their direct application to industrial-scale kilns remains uncertain⁶.

In parallel, radiative heat transfer in combustion environments has received extensive attention since the 1960s. Foundational models derived by Hottel and Sarofim¹⁶, and Siegel and Howell¹⁷, introduced early frameworks that were based on gray-gas assumptions, simplified geometries, and uniform compositions to model gas-phase radiation. However, subsequent work, notably by Modest¹⁸, has expanded these treatments to include non-gray behavior, spectral models, and complex participating media. These developments are especially important for large-scale rotary kilns, where high-

temperature gases such as CO₂ and H₂O dominate radiative heat transfer, and entrained solids such as dust, ash, and char further enhance effective emissivity through particle interactions^{19–21}.

Several numerical studies have attempted to model heat transfer in rotary kilns so as to understand the gas-solid interactions and radiative effects. Early modeling efforts laid the foundation for simulating heat transfer in rotary kilns. Spang²² developed a dynamic 1-D model of a cement kiln using partial differential equations, demonstrating that the flame position and burning-zone temperature can vary significantly under transient conditions. Guruz and Bac²³ set-up a steady-state mathematical model for rotary cement kilns using the zone method in combination with Monte Carlo simulations to analyze the radiative heat transfer and chemical reactions. Key results of that study included the temperature and composition profiles of gas and solids, revealing sensitivity to combustion patterns and residence times, with validation against plant data. The authors concluded that while the model effectively predicted clinker properties (e.g., free CaO content), its accuracy could be improved with additional data on gas flow and particle radiation. Mastorakos et al.²⁴ developed a 2D gas and 1D bed model to study flame structure, radiative transfer, and clinker chemistry, validating their results with outer shell temperature measurements. Similarly, Agrawal and Ghoshdastidar²⁵ proposed a 3D gas and 1D bed model for a rotary lime kiln, examining the axial profiles of the gas and bed temperatures and the degrees of calcination for different rotational speeds and bed conditions, including limestone. Their results showed that lower speeds minimized wall temperature fluctuations and reduced kiln length requirements, although this appeared to come at the cost of lower production rates due to reduction in solids throughput. Mujumdar and Ranade²⁰ developed a 1-D steady-state model that incorporated mass exchange between the gas phase and solids to simulate CO2 release during calcination. The model predictions for the temperature distribution along the gas, solid bed, and kiln wall were validated using temperature measurements reported in previous studies. These studies provide useful computational frameworks that complement experimental investigations, especially for assessing how heating methods and bed materials influence process conditions.

In addition to the numerical studies, several experimental investigations have quantified the temperature and flow behaviors in rotary kilns and drums, particularly for varying bed materials and operating conditions. Boateng²⁶ studied the velocity profiles of particles, including limestone for different fill percentages and rotational speeds, offering insights into active layer dynamics and mid-bed motion. Henien et al.²⁷ examined the transverse velocity profiles of limestone and other materials as functions of the rotational speed, bed depth, and particle properties, presenting diagrams that classified the motion regimes based on operating parameters.

Direct temperature measurements within rotary kilns are less common due to the difficulties associated with obtaining accurate data under extreme thermal conditions and during continuous rotation. However, such measurements are essential for model validation and process optimization. Liu and

Specht²⁸ experimentally assessed the circumferential bed temperature profile in a co-current pilot-scale rotary kiln (length, 6.7 m; outer diameter, 400 mm) fired with natural gas and using a programmable 70-kW burner. They used dry sand as the bed material and embedded thermocouples at various radial positions in the kiln shell, in order to monitor simultaneously the temperatures of the freeboard gas, kiln wall, and bed material. The results revealed minimal circumferential variation in the passive layer and highlighted key zones of thermal uniformity, while also showing substantial radial gradients near the feed end, which diminished with progression along the kiln length. Watkinson and Brimacombe²⁹ studied limestone calcination in a 5.5 m-long, 0.61 m-diameter laboratory-scale rotary kiln fired with natural gas, measuring the axial profiles of the gas, solid, and wall temperatures to evaluate the calcination dynamics. Their work provided some of the earliest direct temperature data linked to material transformation in rotary systems. Butler et al. 30 experimentally investigated radiation heat transfer in a laboratory-scale pulverized coal-fired reactor, measuring the gas and particle temperatures using a triply shielded suction pyrometer and a two-color pyrometer, respectively. Their results highlighted spatial disparities between the gas and particle temperatures and validated discrete ordinates method predictions for radiative fluxes, which were within 8% agreement with the experimental data. Their key findings emphasized the dominance of soot radiation in flame zones and the need for accurate input data (i.e., wall temperatures, particle distributions) for model validation. This work complements the rotary kiln studies by providing benchmark radiative heat transfer data derived under controlled combustion conditions. Jacob and Tokheim³¹ studied a laboratory-scale rotary calciner (length, 2.9 m; diameter, 0.71 m) that was internally heated by three symmetrically placed, axial electrical heating elements, with the goal to explore electrification strategies for high-temperature processes. Operating continuously with a limestone feed, the study combined experimental data with a 1-D OpenModelica model. The key finding was that the current setup had high heat losses of ~60%, resulting in an average heat transfer coefficient of 101 W/(m²K). However, their model proposed that optimizing insulation and residence time could drastically reduce this heat loss to 11%.

While modeling and experimental studies have deepened our understanding of temperature distributions and radiative behaviors in rotary kilns, practical operation requires in addition accurate quantification of energy losses, to allow evaluations of system efficiency and to guide thermal optimization. Heat from the kiln's inner wall is conducted through the refractory lining to the outer shell, where it is dissipated to the surroundings through a combination of convection and radiation. To quantify these heat losses, mass and energy balances are utilized and reported in the literature. Boateng⁷ has reported that in large-scale, industrial direct-fired rotary kilns, radiation and convection losses from the kiln shell typically account for 10%–15% of the total energy input. This range serves as a reference point for evaluating reported losses across various kiln types and scales. For example, Engin and Ari³² conducted an energy audit of a 50-m dry-type cement rotary kiln, reporting that radiation and convection losses from the kiln surface accounted for 10.47% and 4.64%, respectively, of the total energy input. Sögüt et al.³³ evaluated

heat recovery in a cement plant rotary and found that 5.1% of the input energy was lost due to inefficiencies in the existing heat recovery mechanisms, although surface losses were not explicitly detailed. Nasution et al.³⁴ analyzed the rotary kiln unit at an Indonesian cement plant and observed that approximately 30.8% of the energy input was lost, resulting in a thermal efficiency of 69.2%. Ustaoglu et al.³⁴ studied a wet-type rotary kiln and found that energy losses reached 54%, attributed primarily to the exhaust gas stream with almost 30.5 MW of recoverable heat, underscoring the need for energy integration.

With regards to energy inefficiency, air leakage has been identified as a major issue, in that it adversely affects thermal performance, fuel consumption, and emissions³⁵. These leakages occur predominantly at the kiln inlet and outlet seals, where rotating components interface with stationary ducts, making it difficult to achieve airtight conditions. Furthermore, the negative pressure inside the kiln can draw in ambient air through small gaps or worn seals, which leads to excess air that dilutes the combustion gases, affects the flame temperature, and increases the fuel demand. Acharya et al.³⁶ have demonstrated this in their study on hazardous waste incineration kilns, in which air leakage reduces heat transfer to the solid bed. Shahin et al.³⁷ have further explored the impact of excess air in a lime production kiln, modeling the preheater, kiln, and cooler zones. Their results indicate that reducing the excess air from 15% to 10% leads to a 2.5% decrease in fuel consumption, highlighting the operational benefits of minimizing air leakage and optimizing airflow control.

The formation of a coating layer, often termed 'ring formation', along the refractory lining of rotary kilns impacts thermal performance and operational stability. These rings are typically composed of sintered or partially fused raw meal material that adheres to the inner wall of the kiln, especially in regions with specific thermal and chemical conditions. The rings form primarily due to local overheating, chemical reactions (e.g., eutectic melting), material sticking facilitated by high temperatures, variations in feed composition, and fluctuations in the airflow or fuel input. While a thin, uniform coating can serve as an insulating barrier that protects the refractory lining and improves thermal efficiency, excessive or uneven buildup can restrict the material flow, disrupt heat transfer, and lead to unscheduled shutdowns. Early work conducted by Tran and Barham³⁸ in which they examined the effects of excessive coating buildup in rotary lime kilns, found that such accumulations could eventually lead to operational shutdowns due to restricted gas flow and reduced material throughput. However, they also emphasized the beneficial role of a controlled coating layer, in that it acts as a thermal barrier that shields the refractory lining from high gas temperatures and chemical attack, thereby extending its service life and enhancing kiln longevity. Subsequent modeling studies quantified this effect in a more-systematic manner. Ravindran and Krishnan³⁹ used ANSYS Mechanical APDL to simulate clinker-based coatings in different kiln zones, and they found that increasing the coating thickness from 0 to 100 mm reduced the heat losses by more than 50% while lowering the shell temperature to within the desired range of 190°-220°C. Similarly, Akbari et al. 40 applied multiple

identification methods, including Ordinary Least Squares (OLS), Recursive Least Squares (RLS), and genetic algorithms, using shell temperature data and finite element simulations to estimate coating thickness, highlighting that appropriate coating management could prevent refractory erosion and reduce fuel demand. A significant advancement was made by Wirtz et al.⁴¹, who developed a CFDbased "blocked-off region" method to simulate coating regions as solid layers, thereby modulating the momentum and radiative heat transfer characteristics within the kiln. Their simulations showed that the presence of coatings, especially near the sintering zone, significantly increased the fluid velocity (up to three-fold), raised the gas temperature and incident radiation intensity, and altered flame propagation. These effects stem from the insulating nature of the coating, which deflects the burner jet and leads to higher flue gas temperatures exiting the kiln. Singh and Ghoshdastidar²¹ extended this approach by incorporating coating formation, melting, and chemical reactions in a coupled alumina-cement kiln model. They noted substantial axial variations in the wall, gas, and solids temperatures, especially under dust-entrained flow, which affected the thermal efficiency. Recent work by Ryan⁶ has shown that midkiln rings appear whenever the calcination front, i.e., the point where the bed first reaches the calcination temperature, slides a few meters along the kiln; a 4-m shift upstream matched a surge in ring build-up. Their model linked such shifts to two easily monitored factors: fuel-to-production ratio; and feed-mud temperature. Adjusting the fuel rate by about $\pm 10\%$ or the feed temperature by roughly 50° C moved the front a distance of 1-2 m, which is sufficient to initiate or suppress ring formation. This indicates that tighter control of these two variables can help to regulate coating behavior and maintain a stable, beneficial ring thickness that supports thermal performance without causing operational issues.

Our research group at Chalmers University of Technology has been active in the field of hightemperature heat transfer in rotary kilns for nearly a decade, making significant contributions spanning modeling, diagnostics, and experimental validation. The foundation for this work was laid by Klas Andersson¹⁴, whose doctoral work focused on characterizing, using FTIR spectroscopy and narrowangle radiometry, the radiative properties of oxy-fuel combustion flames, particularly the temperature and emissivity levels of coal and propane flames. His work enabled the development of accurate spectral models and provided an essential understanding of gas and soot radiation behaviors¹⁴. Building on this, Daniel Bäckström⁴² conducted detailed in-flame radiation measurements in 400-kW rotary kilns using coal and biomass fuels. He developed experimental systems to measure particle size distributions, soot volume fractions, and radiative intensities, showing that particle radiation dominated gas radiation in coal flames. He also confirmed, through modeling using Mie theory and statistical narrow-band methods, that co-firing biomass altered the radiative transfer length and efficiency, even when maintaining similar peak intensities⁴². Adrian Gunnarsson⁴³ expanded this knowledge base by developing advanced 3D radiative heat transfer models of rotary kilns using the discrete ordinates method, validated against pilot-scale and full-scale data. His models accounted for gas, soot, ash, and bed material radiation and quantified that over 80% of the total heat transferred to the bed was due to radiation. He also showed that fuel choice and combustion setup significantly affected the spatial distribution of heat flux, with coal and biomass co-firing yielding higher fluxes than cleaner fuels¹¹. More recently, Elias Ehlmé focused on modeling the shift from fossil fuels to hydrogen and thermal plasmas in rotary kilns. He developed updated gas radiation models that are suitable for high-temperature ranges (up to 5000 K) and coupled them with CFD simulations to evaluate how electrification alters the heat transfer patterns. His findings showed that hydrogen combustion results in lower radiative transfer due to the absence of particles, suggesting the need for hybrid heating strategies or optimized kiln designs⁴³. Complementing these developments, Fakt et al.⁴⁴ evaluated the feasibility of a full-scale (8 MW_{el}) CO₂ plasma-heated kiln using radiative transfer modeling. Their work showed that the lower radiative output of CO₂ plasma jets can be mitigated by design adjustments such as particle injection or angled torch placement, maintaining clinker production targets. Together, these studies represent a clear research trajectory from experimental measurements of gases and particles in combustion flames to the development of validated computational models of rotary kilns, ultimately enabling advanced simulations of fuel transitions such as hydrogen and plasma heating.

2.4 Thermal plasma

In addition to combustion and resistance heating, alternative electrification strategies should be considered. One promising pathway is thermal plasma, which addresses several of the limitations associated with conventional systems. Thermal plasma systems offer the advantage to high-temperature processes that they can deliver extremely high energy densities and stable thermal environments without the need for conventional fuels. Unlike combustion-based systems, which rely on carbon-intensive reactions and produce soot and particulates that contribute to radiative heat transfer, thermal plasmas involve direct ionization of gases using electric power, enabling combustion-free operation. When powered by renewable electricity, thermal plasmas provide a nearly carbon-neutral heat source, making them an attractive option for electrifying rotary kilns and similar high-temperature reactors.

High-temperature processes are generally defined as industrial operations that require temperatures in excess of 1,000°C for material transformation, melting, decomposition or chemical reactions. These processes include cement clinker production, iron and steel making, glass manufacturing, mineral processing, and thermal waste treatment. Achieving such extreme temperatures with conventional electric heating methods, for example, resistance heating elements or induction heating, remains technically challenging due to limitations related to material stability, thermal transfer rates, and scalability. In this context, thermal plasma technologies are particularly promising, as they are capable of achieving gas temperatures in excess of 10,000 K, thereby enabling intense localized heating and efficient thermal energy delivery even in harsh industrial environments⁴⁵.

Plasma, which is often referred to as the 'fourth state of matter', is an ionized gas composed of free electrons, ions, and neutral particles that collectively exhibit unique electrical conductivity,

electromagnetic interactions, and radiative behaviors⁴⁶. Plasma is formed when a sufficient amount of energy is supplied to a gas, typically in the form of an electric field, causing the atoms or molecules to ionize. This ionization process imparts high thermal energy to the gas and enables it to conduct electricity, respond to magnetic fields, and emit strong thermal radiation. The unique characteristics of plasma make it highly effective for applications that require rapid heat transfer, controlled thermal environments, or the dissociation of stable molecules such as CO₂⁴⁷. Plasmas are generally classified into two broad categories based on their thermodynamic equilibrium conditions: non-thermal (cold) plasmas and thermal (hot) plasmas. In non-thermal plasmas, the electron temperature is significantly higher than the temperature of the ions and neutral gas molecules. These discharges are typically operated at low pressure or in dielectric barrier setups, producing relatively low average gas temperatures (typically <1,000°C), while maintaining high-energy electrons (1–10 eV). Non-thermal plasmas are well suited for low-temperature chemical applications such as CO₂ reforming, hydrogenation, and sterilization, as they allow selective excitation and dissociation of molecules without bulk heating^{48–50}.

In contrast, thermal plasmas operate at close to thermodynamic equilibrium, with all particle species, electrons, ions, and neutral atoms, attaining similar high temperatures, typically ranging from 2000 K to over 20,000 K. This results in extremely high energy densities, heat fluxes, and quenching rates, making these plasma ideal for high-enthalpy applications such as cutting, welding, gasification, surface modification, and thermal spraying^{51,52}. Thermal plasmas are generally categorized as transferred arc and non-transferred arc systems. In transferred arc torches, the arc is formed between an electrode within the torch and an external workpiece, enabling direct energy deposition onto the material. This results in extremely high local power densities and high thermal efficiency, making transferred arc systems highly suitable for metallurgical applications such as metal melting, refining, and plasma arc remelting (PAR). These torches have been widely adopted in the remelting of refractory and specialty alloys, including steel, titanium, and nickel-based materials. For instance, cold hearth melting using transferred arc torches is used in the aerospace industry to produce high-purity titanium by eliminating high-density inclusions (HDIs) and interstitial defects. Plasma arc remelting also allows for controlled solidification using water-cooled copper molds, producing defect-free ingots directly from sponge or scrap metals. Large-scale implementations of transferred plasma arcs include multi-megawatt transferred arc furnaces for direct steelmaking, waste dust melting, and alloy purification, as developed by industry leaders such as Linde and Tetronics. In contrast, non-transferred arc torches house both electrodes within the torch body, retaining the arc internally. The resulting plasma jet exits the torch through a nozzle and is directed either onto a material or into a reaction zone. Although less energy is transferred directly to the target compared to the transferred arc mode, non-transferred arc systems offer greater control, are stability, and versatility, especially for processes that require a sustained hightemperature plasma flow. These processes include plasma spraying, powder synthesis, and hazardous

waste treatment. Non-transferred arc reactors have proven effective for the synthesis of ultrafine powders, such as silicon carbide (SiC), titanium carbide (TiC), and boron carbide (B₄C), which are essential for the production of advanced ceramics and nanomaterials. Furthermore, the closed configuration allows for operation in controlled atmospheres, minimizing contamination and enhancing control of the chemical reactions during material synthesis or waste destruction⁵³.

The selection of a plasma-forming gas crucially influences the plasma properties, heat transfer, and arc stability. Argon (Ar), with its inert monoatomic nature and stable arc, is ideal for thermal spraying and welding. Nitrogen and hydrogen, as diatomic gases, have enhanced thermal conductivities due to dissociation and vibrational modes, making them preferable for high-enthalpy applications, while retaining electrical conductivities comparable to that of Ar⁵⁴. Helium, despite having a higher ionization energy, provides even greater thermal conductivity and diffusivity, promoting broader, more-uniform plasma jets, which are particularly useful in precision heating⁵⁵. Air, as a plasma-forming gas, offers cost-effective operation and wide availability, though its lower thermal conductivity and complex dissociation behavior (due to nitrogen and oxygen) can limit the heat transfer efficiency, as compared with noble or molecular gases. In addition, operation with air can lead to significant NO_x formation, which raises environmental and process-related challenges. Air is commonly used in arc cutting, surface treatments, and waste processing applications. Pure CO₂ plasmas, with strong molecular emissions across the mid-infrared wavelengths, are effective for radiative-dominated heating processes, including thermal conversion and material synthesis ⁵⁶. Gas mixtures offer tailored advantages. For instance, Ar-CO₂ blends combine the arc stability of Ar with the infrared-active molecular bands of CO₂, thereby enhancing radiative heat transfer. Moreover, CO2-CH4 mixtures support reducing environments and efficient radiative energy outputs for processes such as ilmenite reduction⁵⁷. Moreover, CO₂–CH₄ mixtures support reducing environments and efficient radiative energy outputs for processes such as ilmenite reduction⁵⁸.

The performance of thermal plasma torches depend on a range of factors, including electrode geometry, gas composition, arc stability, and the precise control of flow rate and electrical power⁵⁹. These parameters not only influence the arc characteristics but also directly affect the temperature field, energy density, and radiative output of the resulting plasma jet. In the context of rotary kilns, where plasma torches can be used to heat a moving bed of cement raw material, it becomes essential to quantify both the temperature distribution and radiative heat transfer of the plasma plume. Accurate characterization of these properties is crucial for assessing the feasibility and efficiency of plasma-based kiln operation.

Early industrial-scale work carried out by Bonizzoni and Vassalloa⁶⁰ showed that DC non-transferred thermal-arc torches up to 6 MW, operating at ~30,000 K, could crack halogenated liquids and vitrify solids with destruction and removal efficiencies (DREs) of up to 99.999996% for printed circuit boards (PCBs) and deposit protective ceramic coatings at a thickness of 0.05–0.5 mm in a single pass;

continuous stack-gas/water analyses quantified these figures and underlined the cost-competitiveness of plasma once transport is included. Gleizes et al.⁶¹ presented a unified local thermal equilibrium (LTE)/non-LTE computational fluid dynamics (CFD) framework for wall-stabilized, free-burning, and transferred DC arcs that were validated against measured voltage drops and classical Elenbaas-Heller temperature profiles; their analysis showed that in the hottest arc, core radiation is usually the dominant energy-loss factor, and that for air an optical thickness of just 1 mm is sufficient to reabsorb roughly 90% of the resonance-line photons. The accompanying plots indicated that the net-emission coefficient decreased by about two orders of magnitude relative to an optically thin column of the same temperature. Murphy and Park⁶² demonstrated using fully coupled 3D models of MIG welding arcs, inductively coupled jets and AC circuit-breaker arcs that neglecting two-way plasma-surface feedback (metal-vapor cooling, droplet pinch-off, wall ablation) can lead to mispredictions of weld-pool shape, arc attachment and breaker voltage, emphasizing the need to model simultaneously the radiative, convective, and conductive exchanges. Extending the modeling to rotary equipment, Ko et al. 63 inserted three 23.7-kW N₂ non-transferred torches into a cement kiln and, with renormalization group (RNG) kε/P-1 CFD, showed that the torch plume created a local 4,000-K zone that stabilized the bulk gas at ≈2,300 K and guaranteed full SF₆ pyrolysis to CaF₂ within the first 0.5 m of the kiln. At the arc-physics scale, Villarreal-Medina et al. 64 compared 200-A, 10-mm GTAW arcs in nine gases and found, using 2-D LTE simulations with Gibbs-minimized thermodynamic data, that Joule heating was strongest near the cathode, particularly in Ar, while helium transported the highest level of energy convectively to the anode. Radiation increases but peaks in Ar, with CO2 sitting mid-range rather than being radiationdominated. Fluorine arcs lose the largest share of energy through conduction, owing to their steep anode-side temperature gradient. Moving to waste-to-energy, Zhou et al. 65 investigated plasma gasification of incinerator fly-ash and municipal sludge in a pilot furnace equipped with three 120-kW DC air torches (non-transferred arc) serving as the sole heat source. A 3-D Fluent CFD model, pressurebased solver with Realizable k-ɛ turbulence, P1 radiation, and water-evaporation/surface-reaction chemistry predicted a melting-zone (plasma-core) temperature >4,000 K, derived from the center-line contours of the simulated temperature field. Zhang et al. ⁶⁶ developed a time-resolved, 2-D multiphysics model for an Ar CMT + pulse arc. The solver predicts predicted CMT-phase core maxima of 17,700 K and 19,100 K, while the 280 280-A pulse drives drove the column to a temperature of 34,600 K, then down to 20,500 K. High-speed images captured at 1, 5, 15 and 20 ms closely matched the simulated arc contours, corroborating confirming that a shorter electrode gap intensifies the current density and pushes anode-side temperatures above 8000 K almost concomitantly with the square-wave current. Fakt et al. 44 evaluated the feasibility of using an 8-MW thermal plasma torch with CO₂ as the working gas to replace fossil fuels in cement rotary kilns. They addressed the challenge of reduced radiative heat transfer in plasma-heated systems by modeling strategies that involved tilting the plasma toward the bed and injecting particles to enhance heat transfer. They demonstrated that combining these methods with optimized kiln dimensions and feed rates achieved the clinkerization temperature (1,450°C) while reducing the flue gas temperature to ~1,200°C. That work highlights the potential of plasma electrification to cut 40% of the CO₂ emissions from cement production, although further validations of the temperature profiles and bed dynamics are needed.

Turning now from numerical predictions to hands-on investigations, experimental campaigns over the past two decades have mapped real plasma properties and process performances across a wide range of torch configurations and applications. Yugeswaran et al.⁶⁷ experimentally characterized the atmospheric-pressure Ar jet from a non-transferred DC plasma-spray torch that was developed for coating and powder processing. The electron density was derived from Stark broadening of the Ar I 430-nm line, and the jet temperature from a 10-line atomic Boltzmann plot recorded with an opticalfiber probe positioned 2 mm below the nozzle and scanned axially to 6 mm. At that 2-mm plane the excitation temperature rose with the input power from 6500 K (8.1 kW) to 9200 K (16.3 kW), and extrapolation indicated nozzle-exit values in the range of 7300-9200 K. Both temperature and electron density decayed downstream as turbulent entrainment cooled the plume. Since increasing the Ar flow altered these metrics only slightly, it was concluded that torch power, rather than gas flow, is the dominant factor for controlling heat-transfer capacity in argon plasma jets. Hrabovský et al. ⁶⁸ performed experimental plasma-gasification campaign in which a 130-140-kW water-stabilized DC arc torch generated a high-enthalpy steam/Ar jet to react incoming biomass or plastics with added CO₂ (and/or O2). Calorimetric energy balances on the torch's cooling circuit gave a bulk plasma temperature of 15,500 K and a mean enthalpy of 149 MJ kg⁻¹. Power-balance charts showed that most of the input was consumed by CO2 dissociation, yet the resulting H2-CO syngas had a lower heating value that was up to twice the torch power and contained <10 mg Nm⁻³ tar, underscoring the efficiency of the waterstabilized arc for high-quality syngas production. Wang et al.⁶⁹ carried out an experimental study of a six-cathode DC helium torch (200-300 A, 10-20 kW) that was intended for zirconia spraying. The corejet temperature was obtained from the specific enthalpy measured using a water-cooled, three-tube probe, which converts the cooling-water heat gain into plasma enthalpy and then temperature via energy-balance equations. With the arc current and input power fixed, the probe data showed the core temperature falling from 19,330 K to 16,020 K as the gas flow increased from 15 slm to 35 slm, demonstrating the cooling effect of the higher mass flow on the helium jet. Yang et al. 70 examined plasma-assisted CO2 splitting for fuel production, by operating a 12-kW, double-anode DC arc fed with an Ar/CO₂ mixture and followed by a novel supersonic-quench section. They first estimated the equilibrium temperature at ≈3,050 K from a zero-dimensional enthalpy balance that combined input power and a measured electro-thermal efficiency of 70%. To characterize heat transfer, they coupled bench tests with a 2-D compressible FLUENT k-ω model, showing that the converging nozzle plus the water-cooled tube produced quench rates of 10⁷ K s⁻¹, driven mainly by adiabatic expansion and intense convective mixing against the cooled wall, which were fast enough to freeze the high-enthalpy CO + O₂ products before recombination. Under these conditions, the reactor achieved 33% single-pass CO₂

conversion with a net energy efficiency of 17%, indicating that rapid quenching is a decisive factor in making thermal-plasma CO₂ pyrolysis energetically viable. Amarnath et al.⁴⁷ experimentally characterized a rod-cathode/nozzle-anode DC non-transferred torch that operated with an Ar/CO₂/CH₄ mixture at 1 atm. Optical-emission spectroscopy measured jet temperatures that climbed from 13,400 K at 100 A to 17,800 K at 200 A, and calorimetric balances gave a 73% electro-thermal efficiency at 100 A with 15 slpm Ar + 20 slpm CO₂ + 6 slpm CH₄. Under these conditions, the 15-kW plume spheroidized 85% of the 10–60-um tungsten powder in a single pass, confirming the torch's suitability for rapid processing of carbon-rich materials. Galaly et al.⁷¹ experimentally characterized a 125-kW non-transferred DC air torch designed for plastic-waste gasification. The jet temperature was measured 2-5 mm downstream of the nozzle by recording the emission spectrum with an AvaSpec-2048 fiber probe, locating the intensity peak, and converting λ max with Wien's displacement law, which gave 15,000-19,000 K as the air flow increased from 10 g s⁻¹ to 30 g s⁻¹ at 100-250 A. The spectral data showed that a higher flow cooled the plume (\lambda max red-shifts), while current-voltage traces confirmed that torch power, and not gas mass-flow, governs enthalpy delivery. This convective cooling could be countered by increasing the current, yielding jet velocities of up to 2.8 km s⁻¹ and sustaining the heat flux needed for complete plastic cracking; an overall energy-conversion efficiency of 81% for the plastic-to-fuel route reinforces the potential of the torch for waste-to-energy schemes. In addition to their use in waste treatment, material processing, and high-temperature synthesis, transferred arc plasma systems have potential applications in metallurgical processes, particularly for fossil-free steel production through hydrogen plasma smelting reduction (HPSR). A series of experimental investigations carried out at Montanuniversität Leoben has demonstrated the viability of using DC transferred arc plasmas with H₂/Ar gas mixtures to directly reduce iron ores under extreme thermal conditions. Badr⁷² developed a HPSR process using a DC transferred arc with continuous ore feeding through a hollow graphite electrode. Experiments achieved slag bath temperatures of 1,400°-1,500°C and reduction degrees >90%. The use of CH₄ gave 3.5-4.0-times greater reduction rates than H₂, and coke addition suppressed FeO in the slag. Empirical equations were derived for specific reduction rates at plasma temperatures estimated to be close to 2,400°C. Building on this, Zarl et al. 73 used a 5-kVA DC arc system to define experimentally the stability fields by varying the voltage, current, arc length, and gas composition (Ar, H₂, N₂, and mixtures). Their findings showed that increased hydrogen content narrowed the operational stability range, and that ore injection had a destabilizing effect on the arc, providing information that is critical for reactor scale-up. Ernst et al. 74 used an Ar-H₂ DC plasma and employed gas mass spectrometry and electrical diagnostics to investigate the influences of the ore feed rate into a molten slag bath and gas composition, achieving hydrogen utilization efficiencies of >80% under optimal charging conditions. Using Bauer-Glaessner equilibrium diagrams, the localized plasma temperature in the reaction zone was estimated to reach ~3,025°C, reinforcing the system's capability to sustain rapid high-temperature reduction under controlled plasma conditions. Pauna et al. 75 integrated synchronized optical emission spectroscopy and high-speed imaging to observe the arc plasma

behaviors in HPSR. By analyzing the Fe I and Fe II emission lines in Boltzmann plots, they determined that the plasma temperatures within the iron vapor-dominated arc region were in the range of 4,000–5,500 K. These measurements enabled spatial mapping of energy distribution and spectral dynamics, supporting real-time monitoring of reduction conditions and arc stability.

In addition to thermal and radiative characterizations, the morphological behavior of plasma jets, particularly the occurrence of necking, have been documented in high-current plasma focus systems. These systems often exhibit axial plasma jets that originate from Z-pinch-induced necking within the electrode region. Polukhin et al. ⁷⁶ demonstrated that this necking results from strong magnetic self-compression during pinch formation, acting like a nozzle that ejects dense, high-velocity plasma jets. Further investigations by the same group ⁷⁷ using kilojoule-scale facilities confirmed this mechanism using laser interferometry. Auluck et al. ⁷⁸, in a comprehensive review of plasma focus research, corroborated these findings and reported repeated observations of necking structures and associated jet formation across multiple Plasma Focus devices worldwide. While such necking is typically observed internally within the discharge chamber, the present study shows radial constrictions in the visible plasma plume of a non-transferred DC arc system, which may represent an analogous phenomenon, although the underlying mechanisms could differ.

The transition from fossil-fueled combustion to electrified systems, such as thermal plasmas, fundamentally alters the radiative and convective environments within rotary kilns. While these systems offer the promise of high-temperature, combustion-free operation, they introduce uncertainties in relation to heat transfer behavior. In particular, the lack of experimental data on axial radiative intensity and flux distributions and plasma-specific transfer characteristics limits our ability to validate and scale emerging models. Moreover, most studies to date have focused on modeling assumptions or low-power setups, with few addressing the conditions relevant to industrial-scale kilns. These gaps highlight the need for experimentally grounded insights into plasma-driven heating. The following chapters address this need by exploring how thermal plasmas and other fossil-free systems influence heat transfer, energy losses, and scalability in rotary kilns.

3. Method

For the experimental work presented in this thesis, a pilot-scale rotary kiln, referred to as Kiln Zero, was employed to investigate the heat transfer conditions under controlled and industrially relevant settings. Kiln Zero, which is located at the Heidelberg Materials R&D facility in Slite, was designed as a scaled-down representation of a cement rotary kiln, enabling systematic studies of different heating methods and raw materials. In parallel, a DC non-transferred arc thermal plasma generator, operated with pure CO₂ as the plasma-forming gas, was employed to produce high-temperature plasma jets for studies of radiative heat transfer, jet geometry, and plasma-material interactions under industrially relevant conditions. Kiln Zero offers flexibility with respect to heating methods, access for diagnostic instrumentation, and compatibility with various material properties, enabling detailed exploration of thermal processes relevant to cement production and electrification. The overall methodological framework is illustrated in Figure 2, which shows how the research questions (RQ1–RQ4) are linked to the experimental work and subsequent analyses, leading to the appended Papers I–III.

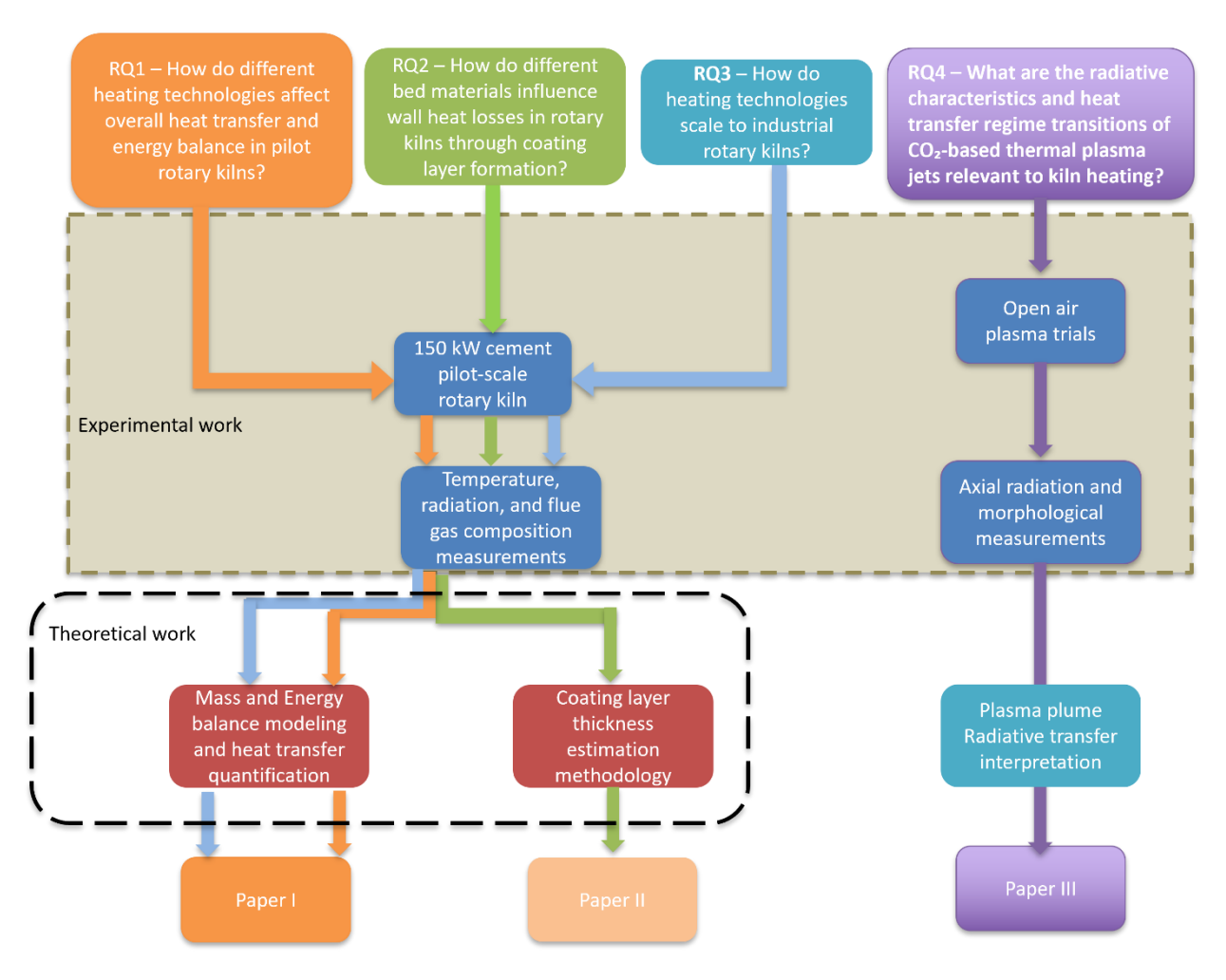


Figure 2 Overview of the methodological framework of this thesis. The research questions (RQ1–RQ4) guide the experimental work in the pilot-scale kiln and in the plasma trials. The resulting measurements form the basis for the energy balance and coating layer analyses, as well as plasma radiative characterization, leading to Papers I–III.

3.1 Experimental setup of Kiln Zero

Kiln Zero, shown in Figure 3, is a custom-built pilot-scale rotary kiln that is designed to emulate the thermal behaviors of industrial cement kilns under controlled and flexible laboratory conditions. The kiln consists of a cylindrical steel with length of 2,925 mm, an outer diameter of 710 mm, and an inner diameter of 580 mm. The steel shell is 10 mm in thickness and is lined with 55 mm of refractory material, allowing it to withstand the high temperatures required for calcination and clinker formation. The kiln is slightly inclined and capable of rotating at adjustable speeds, driven by a motorized system that replicates the continuous tumbling of bed material that occurs in full-scale rotary kilns. At the lower end of the kiln, the wall takes on a conical shape, and four evenly spaced outlets are positioned to allow for the discharge of bed material. The higher end of the kiln serves a dual function as both the material feed inlet and the flue gas outlet. Along the longitudinal axis of the kiln, five measurement ports (P1– P5) are installed, numbered in the direction of the flame and flue gas flow from the burner opening toward the flue gas outlet (see Fig. 3b). These ports are strategically placed to enable access for diagnostic purposes along the kiln axis. The kiln is housed indoors, ensuring stable boundary conditions by shielding the system from external weather influences such as wind and rain. To facilitate continuous feeding of raw material, a dedicated feeding system has been developed and integrated with the kiln (see the right-hand side of Fig. 3a). This system comprises a large hopper that can be filled from big bags, a screw feeder that regulates the flow of material into a smaller intermediate bin, and a chute through which the material is delivered into the kiln's upper end. For certain fine materials, manual feeding was also employed to minimize material losses through entrainment by the exhaust gases. The kiln was operated using two primary heating configurations during the experimental campaigns. In the combustion setup, a burner was positioned at the lower end and supplied with propane gas. The burner was equipped with three separate registers to control the flows of propane, axial air, and radial air. In some experiments, oxygen-enriched combustion was facilitated by injecting additional oxygen through the radial air inlet, in order to achieve higher local flame temperatures. Due to the fixed nature of the burner and the rotation of the kiln shell, there was a small gap between these two elements, resulting in unavoidable leakage of air into the system.

As an alternative to combustion, the kiln was operated with electrical resistance heating. In this configuration, three silicon carbide heating elements were installed longitudinally inside the kiln, each with a length of 2.6 m and a diameter of 55 mm. These elements were arranged in a triangular configuration with 75-mm spacing, to ensure uniform thermal exposure of the bed material (see Fig. 3c). The heating elements, which had a typical emissivity of 0.88, were capable of delivering up to 150 kW of electrical power, matching the design capacity of Kiln Zero. Temperature control was achieved in two stages: (i) an automated phase that regulated the current so as to ramp up the temperature gradually and prevent thermal shock; followed by (ii) manual adjustment of the power to maintain steady-state operation. The inner dimensions of the kiln remained unchanged across the two heating

configurations, ensuring consistent test conditions. Overall, Kiln Zero provided a versatile and instrumented platform to study thermal behaviors, material processing, and energy efficiencies in a rotary kiln environment that is representative of industrial cement production.

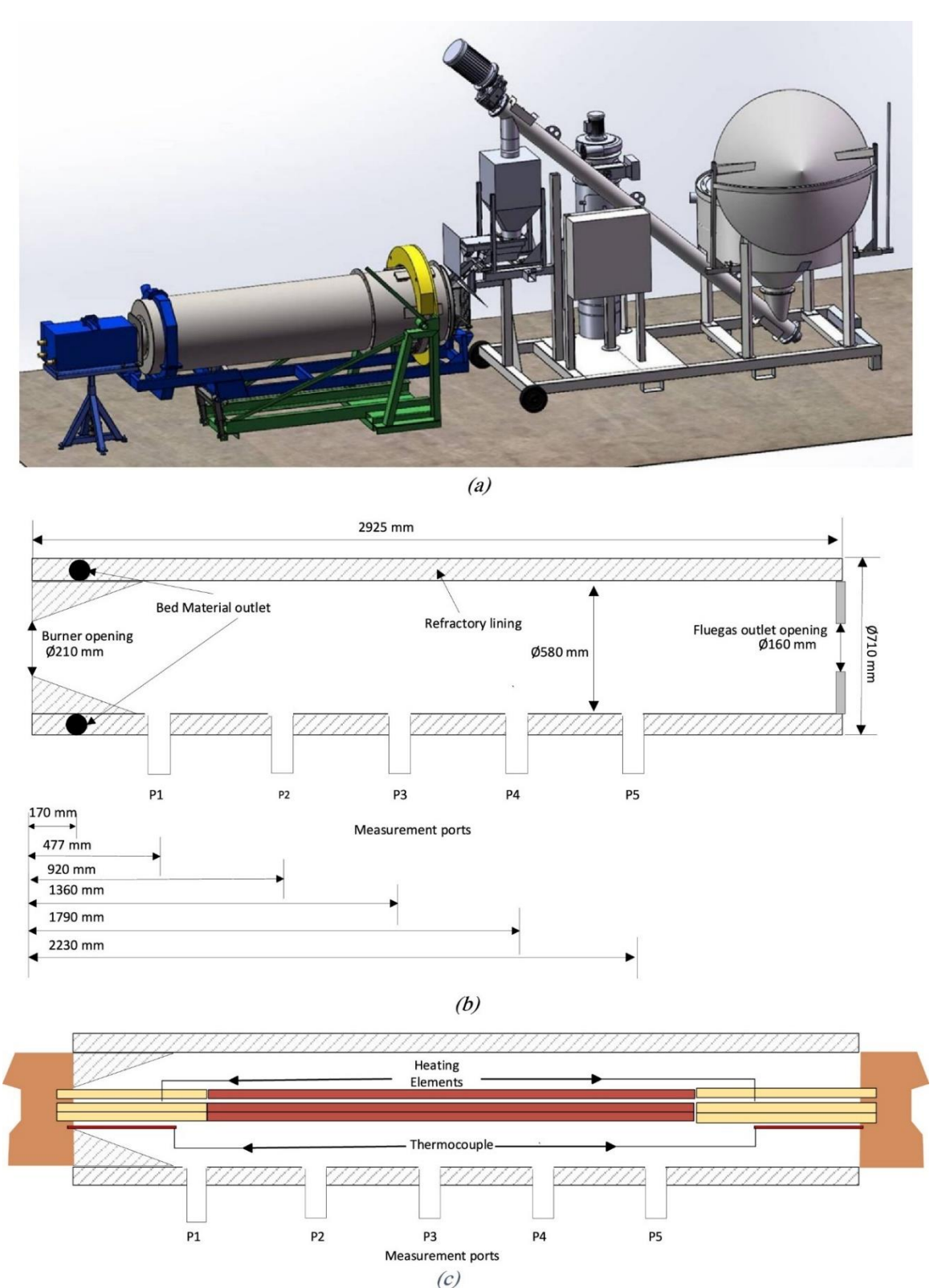


Figure 3 (a) A 3-D model representation of Kiln Zero with the feeding system used during the experimental campaigns. (b) Dimensions of Kiln Zero operated with a propane burner. (c) Kiln Zero with resistance heating elements as heat source.

3.2 Experimental setup of DC non-transferred CO₂ plasma system

Two customized DC non-transferred arc plasma torches were employed to generate CO2 plasma jets in open air for experimental investigations at two power scales: a 50 kW_{el} system and a scaled-up 300 kW_{el} system. Both torches followed the same operating principle, based on a DC hollow electrode design that consisted of a water-cooled copper cathode and anode, separated by an insulating spacer. These components formed the arc channel through which the high-temperature CO2 plasma was generated. To initiate the arc, a high-voltage, high-frequency (HVHF) igniter was used, creating a stable pilot arc under a controlled CO2 gas flow. The arc was then sustained and stabilized using a continuous CO₂ flow regulated by mass flow controllers. The water-cooling system for the torch was designed with internal channels, which effectively dissipated the heat from the electrodes during extended operation, ensuring thermal stability and structural integrity. The 50-kWel torch had a nozzle diameter of 10 mm and an electrode shell diameter of 20 mm, whereas the 300-kWel torch featured a larger geometry, with a 20-mm nozzle diameter and a 70-mm electrode shell diameter, allowing for a greater arc cross-section and higher power delivery. A schematic of the 300-kWel setup, including the torch and diagnostic arrangement, is shown in Figure 4. Note that details of the diagnostic tools are given in the following sections. The electro-thermal efficiency (η) of the torch is determined by measuring the heat losses through the cooling water and is expressed as:

$$\eta = \frac{P_{in} - Q_{loss}}{P_{in}} \times 100 \tag{1}$$

where, P_{in} is the electrical energy and Q_{loss} is the energy dissipated through the cooling water of the plasma generator. The electrical input power is calculated as:

$$P_{in} = U_{arc} . I_{arc} (2)$$

where U_{arc} and I_{arc} represent the arc voltage and current, respectively.

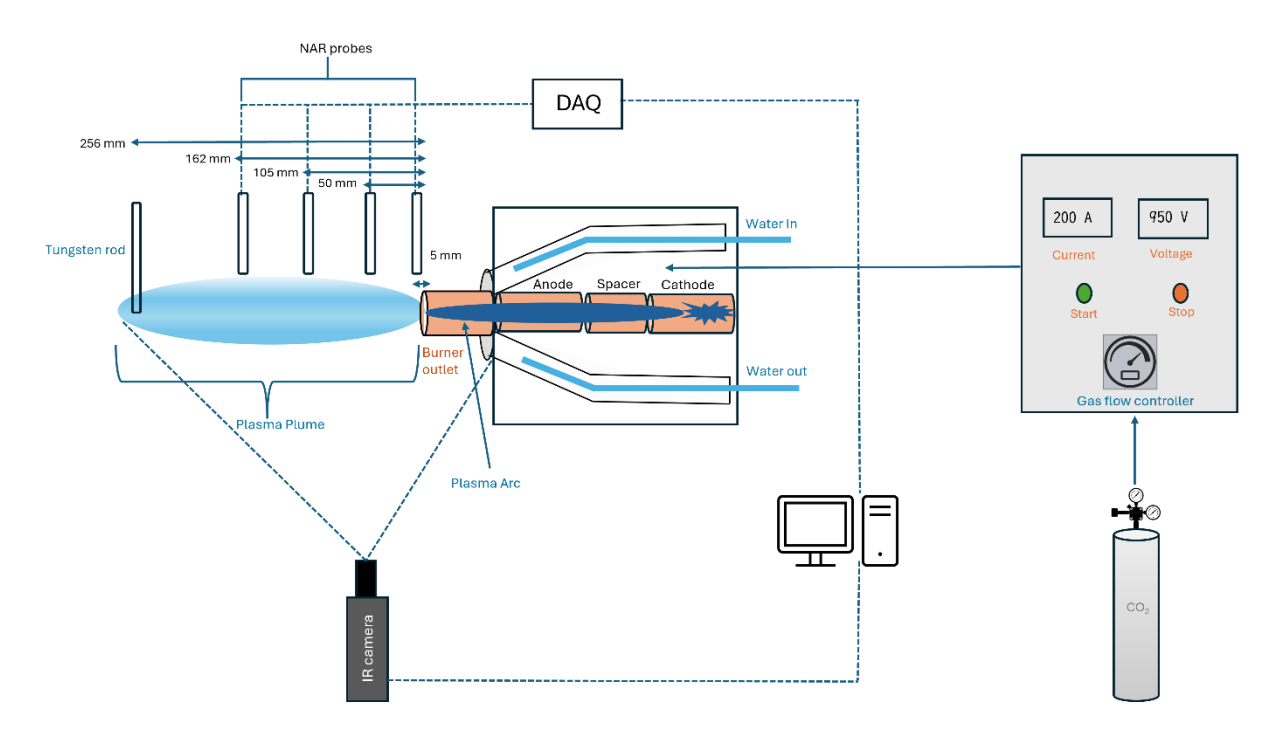


Figure 4 Schematic of the 300-kWel thermal plasma torch and experimental setup.

3.3 Measurement Techniques

To elucidate the heat transfer conditions, radiative properties, and temperature distributions in both the rotary kiln and open-air plasma systems, a range of diagnostic instruments was employed. These measurements were essential for characterizing the thermal environment within each setup and for evaluating the effectiveness of the studied CO₂ plasma.

3.3.1 Narrow Angle Radiometer (NAR)

Radiative intensity measurements were performed using a narrow-angle radiometer (NAR), which is a line-of-sight instrument that has been employed extensively in previous high-temperature studies 11,42,79,80. For measurements performed in the harsh thermal environment inside the rotary kiln, a robust, water-cooled NAR probing system was used. This consists of a titanium probe of approximately 2.3 m in length, with an internal diameter of 1 cm, housing a thermopile sensor with a spectral range of 0.1-100 µm at the back end. Based on the probe geometry, the instrument has a very narrow view angle corresponding to a solid angle of 9.5 × 10⁻⁵ sr. Incoming radiation travels through the narrow inner passage and is focused on the sensor, allowing only light within a narrow solid angle to be detected. The resulting voltage signal corresponds to the directional radiative intensity and is calibrated against a high-precision black-body furnace before and after each measurement campaign. The titanium construction helps prevent mechanical deformation at high temperatures, and a small nitrogen purge flow is introduced into the optical path to prevent gas or particle intrusion. Separate cooling loops are applied to the probe and sensor housing to maintain a stable operating temperature throughout the measurement. This NAR was used in Papers I and II.

For the open-air plasma jet experiments in Paper III, a miniaturized version of the same instrument was used. This compact NAR probe operates on the same measurement principle, utilizing the same thermopile sensor and line-of-sight detection approach, but has a reduced length of approximately 50 cm and is used in such a way that cooling is not required. The smaller size makes it suitable for close-range positioning near the plasma jet, allowing for flexibility in traversing different axial locations while capturing accurate radiative intensity data. Despite its simple design, the miniaturized NAR maintains the measurement fidelity required for analyzing directional radiation from the plasma plume under open-air conditions.

3.3.2 Ellipsoidal radiometer

To measure in a non-invasive manner the incident radiative heat flux to the furnace wall, an ellipsoidal radiometer was used. This instrument is positioned at the tip of a probe and aligned with the inner wall of the furnace, to allow accurate measurements of radiative heat transfer directed towards the wall surface. The ellipsoidal radiometer features a wide view angle, close to 2π steradians, which means that it can capture radiation from almost the entire hemispherical field around the measurement point. The incoming radiation is focused by an ellipsoidal reflector onto a thermopile sensor, and the resulting voltage signal is proportional to the local incident radiative heat flux. This setup enables the determination of the radiative heat transferred from the entire hot gas volume and refractory surroundings to a small, localized point on the wall. As the probe does not intrude into the flow or disturb the thermal field, it offers a reliable means of quantifying wall heat fluxes under high-temperature conditions. This instrument was used in Paper I. Since the measured wall heat flux corresponds to the thermal load experienced by the bed surface, it is a particularly important measure for evaluating kiln heat transfer.

3.3.3 InfraRed thermography (IR)

Infrared thermography was employed to visualize the thermal distribution and monitor the surface temperatures within the experimental setups. The FLIR A655SC infrared camera was used for this purpose, as it is capable of measuring temperatures of up to 2,000°C, with a spatial resolution of 640 × 120 pixels and a sampling frequency of up to 200 Hz. The camera operates in the long-wave infrared region, with a spectral sensitivity range of 7.5–14.0 µm, making it suitable for capturing radiative emissions from high-temperature surfaces, such as combustion flames, plasma jets, and furnace walls. The camera was positioned outside the system ports to acquire thermal images without disturbing the flow or temperature field. Post-processing and temperature extraction were performed using the FLIR ResearchIR Max software, which enabled frame-by-frame analysis, region-based averaging, and thermal mapping. In case of Kiln Zero experiments, a fixed emissivity value of 0.95 was applied during the image analysis, selected based on the surface characteristics of the materials observed and the controlled radiative environment, which closely resembled a blackbody. The infrared camera

provided valuable spatial and temporal insights into the heat distribution across different heating methods used in this study. This equipment was used in Papers I, II, and III.

3.3.4 Fourier-Transform Infrared Spectroscopy (FTIR)

To quantify the gas compositions within the furnace and flue gas stream, Fourier-Transform Infrared Spectroscopy (FTIR) was employed. Gas samples were extracted from multiple kiln ports (P2–P5) and the flue gas outlet, and analyzed using the MKS MultiGas 2030 FTIR spectrometer. This instrument measures gas concentrations by detecting absorption at specific infrared wavelengths within a small optical cell, converting the raw signal into a spectrum via Fourier transform, and comparing the result to an extensive reference database of gas species. The FTIR system operates at spectral resolutions in the range of 0.5–128.0 cm⁻¹, and it allows for up to five scans per second at the highest resolution. In the present study, it enabled reliable detection and quantification of the key gas species, particularly H₂O, CO₂, and CO, which predominate in combustion environments and are relevant due to their radiative and environmental significance. Gas extraction was conducted using a water-cooled sampling probe to protect the probe body from high flame temperatures. To prevent the condensation of water vapor within the system, which would compromise measurement accuracy, the probe included an electrically heated inner tube that maintained the extracted gas stream at a temperature of approximately 200°C.

In parallel with FTIR, the HORIBA PG-250 gas analyzer was used to complement the gas composition analysis. This instrument utilizes chemiluminescence for NOx detection, nondispersive infrared (NDIR) absorption for SO₂, CO, and CO₂, and a galvanic cell for O₂ measurement. The PG-250 gas analyzer offers high repeatability of $\pm 0.5\%$ full scale (F.S.) for NOx (>100 ppm) and CO (>1,000 ppm), and $\pm 1.0\%$ F.S. for other species, with a typical response time of about 45 seconds. Together, the FTIR and HORIBA systems provided detailed, real-time insights into the combustion and gas-phase behaviors across the different heating configurations used in this study. Both items of equipment were used in Paper I.

3.4 Measurement method and operational parameters

The operational parameters and measurement strategies for all three experimental campaigns are outlined in this section. Tables 1 and 2 summarize the bed material compositions and the corresponding operating conditions for the experiments performed in the Kiln Zero rotary kiln. Four distinct bed materials were tested: two raw meals (RM1 and RM2) with feed material sizes <100 µm, and two types of limestone (LS1 and LS2) with feed bed sizes in the range of 5–8 mm. Each material had a different composition, and in some cases, the material was tested under varying operational conditions, as indicated in Table 2, with the label 'set'. As shown in Table 1, CO₂ and SO₃ are included as components of the raw material composition. It should be noted that these values are derived from Loss on Ignition (LOI) tests, representing the mass loss associated with the thermal decomposition of carbonates (CO₂)

and sulfates (SO₃) during heating. These values correspond to the gas released upon thermal treatment and can be back-calculated to their respective original compounds, e.g., CaCO₃ and CaSO₄, for further analysis.

Table 1. Chemical compositions of the bed materials used in the experimental campaigns.

	RM1	RM2	LS1	LS2
%	44.5	42.9	53.0	54.7
%	12.9	13.1	1.81	0.40
%	1.57	3.36	0.68	0.16
%	3.07	1.89	0.32	0.06
%	1.19	2.85	1.20	0.47
%	0.38	0.82	0.19	0.03
%	0.16	0.22	0.06	0.05
%	37.0	34.6	44.3	45.7
%	0.33	1.07	0.13	0.04
	% % % % % % % % % % % % % % % % % % %	% 44.5 % 12.9 % 1.57 % 3.07 % 1.19 % 0.38 % 0.16 % 37.0	% 44.5 42.9 % 12.9 13.1 % 1.57 3.36 % 3.07 1.89 % 1.19 2.85 % 0.38 0.82 % 0.16 0.22 % 37.0 34.6	% 44.5 42.9 53.0 % 12.9 13.1 1.81 % 1.57 3.36 0.68 % 3.07 1.89 0.32 % 1.19 2.85 1.20 % 0.38 0.82 0.19 % 0.16 0.22 0.06 % 37.0 34.6 44.3

RM, Raw meal; LS, limestone type.

Table 2: Operational conditions used for the reference propane case, oxygen-enriched case (clinker), and resistance heating element case (electrified).

Bed material	RM1	RM2	RM2	RM2	LS1	LS1	LS2	LS2	LS2
		set 1	set 2	set 3	set 1	set 2		Clinker	Electrified
Bed feed [kg/h]	50	30	50	50	30	50	45	40	45
Propane feed	2.3	2.4	2.19	2.17	2.84	2.7	2.87	3.32	-
[g/s]									
[kW]	106	111	102	100	132	125	134	154	
Electrical input	-	-	-	-	-	-	-	-	140
[kW]									
Radial air feed	6.3	6.1	5.2	5.2	11.6	5.7	12.8	11.2	-
[g/s]									
Axial air feed	15.3	17.1	15.1	16.2	13.4	16.4	16.6	13.6	-
[g/s]									
Rotation [rpm]	3.3	3.3	3.7	2.7	4.0	2.7	2.7	3.8	3

Table 3 presents the operating conditions used in the open-air plasma experiments. The 50-kW_{el} plasma torch was operated under a single condition (Case A1), while the 300-kW_{el} torch was tested across a broader range of 100–300 A (Cases B1–B10), enabling detailed characterization of the plasma jet under different power inputs.

Table 3: Plasma torch operating parameters for the 50 kW_{el} and 300 kW_{el} torches.

Case Id	Current (A)	Voltage (V)	Gas flow	Efficiency	Effective
			(nm^3/h)	(%)	power (kW)
A1	50	1038	12	83	43
B1	100	1000	30	-	100
B2	150	930	30	89	140
В3	150	1020	40	89	153
B4	200	950	40	87	190
B5	250	920	40	86	230
B6	200	1030	50	87	206
B7	250	995	50	86	249
B8	300	975	50	85	293
B9	250	1038	55	86	260
B10	300	1000	55	85	300

For the rotary kiln experiments, radiative intensity measurements were performed using a NAR inserted through axial ports P1–P5. Each NAR measurement lasted approximately 30 seconds, capturing steady-state line-of-sight radiation from the gas phase. Incident radiative heat flux to the kiln wall was measured using an ellipsoidal radiometer placed in the same ports, aligned with the inner wall surface to capture the hemispherical radiation. Each heat flux measurement was recorded over a 2-minute interval once the signal had stabilized. Gas composition measurements were conducted at ports P2–P5 and at the flue gas outlet using gas extraction probes connected to the FTIR and HORIBA analyzers. Each gas measurement was performed after ensuring a steady signal for approximately 2 minutes, capturing the concentrations of the key flue gas species under both combustion and resistance heating scenarios. The surface temperatures of the inner and outer kiln walls, as well as the resistance heating elements, were recorded using an infrared camera positioned outside the kiln and aligned with the optical ports. Thermographic data were continuously recorded for about 1 minute for each port and post-processed to estimate the average wall temperatures during steady-state operation.

The degree of calcination was determined by analyzing the mineral compositions of the raw feed and the collected product samples using x-ray diffraction (XRD). Crystal structures were identified through Rietveld refinement, enabling quantitative phase analysis of the mineral content. By comparing the measured amount of CaCO₃ in the raw material to that in the processed material, the extent of decomposition was determined. The degree of calcination was then calculated as the reacted fraction of the initial CaCO₃ content, representing the proportion of the mineral that underwent thermal decomposition during kiln operation. This was done by the Heidelberg Material R&D team.

In the open-air plasma experiments, the plasma jets produced by the two torches exited directly into ambient air, forming high-temperature plumes that extended axially from the plasma generator outlet. For the 300-kWel system, four NARs were placed at fixed axial distances of 5 mm, 50 mm, 105 mm, and 162 mm, respectively, from the torch exit to capture the directional radiative intensity perpendicular to the jet (Fig. 4). In contrast, the 50-kW_{el} system utilized a single NAR probe traversed along the jet axis in 1-cm increments from 1 cm to 14 cm downstream of the outlet. This setup allowed spatial profiling of the radiative intensity along the jet length. Complementary thermal measurements were acquired using an IR camera, positioned orthogonally at the 50-mm axial location (aligned with the second NAR) in the 300-kWel system. A tungsten rod was placed 256 mm downstream of the outlet (Fig. 4), to serve as a visual and thermal reference object; it was located at a sufficient distance to avoid melting while remaining within the jet tail region. The IR camera operated with a fixed emissivity setting of 0.2 and enabled real-time observations of the jet structure, including any localized radial constriction occurring during high-current operation. To quantify this geometry, thermographic data from 500 selected frames per test case were converted into binary images and processed in MATLAB to extract the minimum plume diameter, averaged across all the frames. Prior to plasma ignition, spatial calibration was performed using the known physical distance between the torch and probes to convert the pixel measurements into metric dimensions.

3.5 Mass and energy balance methodology

A mass and energy balance analysis was conducted to quantify the heat losses and energy distribution in the rotary kiln in both the combustion and resistance heating configurations.

The mass balance analysis determined key flow quantities including the flue gas mass flow rate, air leakage (if any), and the extent of calcination. A steady-state, single-zone control volume was defined around the rotary kiln, with the main inputs being the fuel, air, and bed material, and the outputs being the flue gases and calcined solids. The governing equation for the mass balance of the wet flue gas stream is:

$$\dot{m}_{fuel} + \dot{m}_{air} + \dot{m}_{CO_2,calc} = \dot{m}_{fg} \tag{3}$$

where:

- \dot{m}_{fuel} is the mass flow rate of the fuel (measured);
- \dot{m}_{air} is the total mass flow of air (radial + axial + leakage);
- $\dot{m}_{CO_2,calc}$ is the mass of CO₂ produced from the decomposition of CaCO₃; and
- \dot{m}_{fg} is the mass flow of the total flue gases.

To close the mass balance, the stoichiometric ratio (λ) was estimated from the outlet oxygen concentration [O₂] and known values of the degree of calcination (X_{calc}), the molar flow of bed material (n_{CaCO_3}), and the molar flow of fuel (n_{fuel}), assuming that the flue gas consisted primarily of O₂, N₂, CO₂, and H₂O. The following simplified expression derived from combustion stoichiometry was used:

$$\lambda = \frac{5 + 2[O_2] + [O_2] * \frac{X_{calc} n_{CaCO_3}}{n_{fuel}}}{5\left(1 - \left([O_2] + [O_2] * \frac{0.79}{0.21}\right)\right)}$$
(4)

For the resistance heating scenarios, it was assumed that the flue gases consisted solely of CO₂ from calcination, as the kiln was sealed and no combustion took place. Thus, air leakage was negligible, and:

$$\dot{m}_{fg} = \dot{m}_{CO_2,calc} \tag{5}$$

The energy balance was set up to quantify the energy inputs and evaluate the energy losses through the flue gases and kiln surface radiation, and convection. The general form of the first-law balance is:

$$\dot{m}_{fuel}\Delta H_{comb} + \dot{m}_{air}\Delta H_{air} + \dot{m}_{bed\ in}\Delta H_{bed\ in} = \dot{m}_{bed\ out}\Delta H_{bed\ out} + \dot{m}_{fg}\Delta H_{fg} + Q_{conv} + Q_{rad} \tag{6}$$

where:

- ΔH corresponds to the enthalpy change of the respective mass stream relative to the chosen reference temperature T_{ref} and composition. For a fuel ($\Delta Hcomb$), this includes the chemical reaction enthalpy released upon complete combustion, while for air, and for bed material fed in ($bed\ in$), ΔH represents the sensible enthalpy change between T_{ref} and the stream temperature;
- $\Delta H_{bed\ out}$ represents the enthalpy of the bed material as it exits the kiln;
- Q represents the heat losses from the kiln outer surface due to convection and radiation; and
- Subscripts *in* and *out* refer to any mass flows entering and leaving the kiln, respectively, and *fg* refers to the flue gas, which is exhaust gas that exits the kiln.

For electrical heating cases, the energy input was calculated directly from the applied power, as follows:

$$Q = U \times I \tag{7}$$

where U is the measured voltage and I represents the current.

Heat leaving the bed was estimated using the reaction enthalpy and sensible heat, as follows:

$$\dot{m}_{bed\ out} \Delta H_{bed\ out} = \Delta H_{reac} X_{calc} \dot{m}_{bed,in} + \left(C_{pCaO} \frac{M_{CaO}}{M_{CaCO_3}} X_{calc} + C_{pCaCO_3} (1 - X_{calc}) \right) \left(T_{bed\ out} - T_{ref} \right) \dot{m}_{bed,raw}$$
(8)

Radiative and convective losses from the kiln surface were calculated as:

$$Q_{conv} = \frac{k}{D} 0.11\{(0.5 \text{ Re}^2 + \text{Gr})\text{Pr}\}^{0.35} A(T_{outer \, shell} - T_{ref})$$
 (9)

$$Q_{rad} = \varepsilon \sigma A \left(T_{outershell}^{4} - T_{ref}^{4} \right) \tag{10}$$

where:

- $\varepsilon = 0.95$ is the assumed shell emissivity;
- A represents the external surface area;
- $T_{ref} = 300 \text{ K};$
- D is the outer diameter of the kiln;
- *k* is the thermal conductivity of air; and
- *Re*, *Gr*, *Pr* are the Reynolds, Grashof, and Prandtl numbers, respectively (as per Barr et al. ¹⁹ correlations for rotating cylinders).

3.6 Estimation of the thickness of the coating layer

To estimate the thickness of the internal coating layer along the kiln wall, a conduction-based back-calculation method was employed. This approach relies on quantifying the conductive heat transfer through the layered structure of the kiln, which comprises the coating, refractory lining, and steel shell, using measured surface temperatures and known thermal properties. At steady state, all the heat conducted through the wall to the shell (Q_{cond}) must be released to the surroundings. This release occurs entirely via radiation and convection from the kiln surface, such that:

$$Q_{cond} = Q_{conv} + Q_{rad} \tag{11}$$

To determine the conductive heat transfer through the kiln wall system, including the internal coating, the following 1-D steady-state conduction equation was used

$$Q_{cond} = \frac{2\pi L (T_{inner\,wall} - T_{outer\,wall})}{\frac{\ln\left(\frac{r_2}{r_1}\right)}{k_A} + \frac{\ln\left(\frac{r_3}{r_2}\right)}{k_B} + \frac{\ln\left(\frac{r_4}{r_3}\right)}{k_C}}$$
(12)

where:

- *L* is the kiln length;
- k_A , k_B , and k_C are the thermal conductivities of the coating layer (bed material), refractory lining, and outer steel shell, respectively. The shell conductivity k_C is assumed to be 45 W/m·K;
- r_1 , r_2 , r_3 , and r_4 denote the radial positions of the inner surface of the coating, outer edge of the refractory layer (r_2 =0.29 m), outer edge of the steel shell (r_3 =0.34 m), and outer kiln radius (r_4 =0.35 m), respectively; and
- $T_{inner\,wall}$ represent the temperatures at the inner wall (coating surface) and $T_{outer\,wall}$ outer shell, respectively, both of which are measured using infrared thermography.

The thermal conductivity of the refractory lining (k_B) was estimated based on comparative measurements in an empty kiln, yielding an average value of approximately 0.8 W/m·K. The conductivity of the coating layer k_A was not measured directly due to material variability, although its impact is reflected in the final thickness estimate.

4. Selected Results and Discussion

This chapter presents and discusses the results from three distinct experimental campaigns conducted during the course of the work for this thesis. The first set of experiments studied the heat transfer, energy efficiency, and coating effects in a pilot-scale rotary kiln, comparing conventional propane combustion, oxygen-enriched combustion, and electrical resistance heating, followed by a scaling analysis to industrial kilns. The second set characterized CO₂-based thermal plasma in open air, mapping its radiative intensity and heat transfer behavior prior to kiln integration. While each study provides valuable standalone insights, together they form a bridge between the established kiln operation principles and novel applications of high-intensity plasma heating, illuminating a pathway towards electrified, low-carbon cement production.

4.1 Experimental studies in Kiln Zero

The kiln experiments were designed to provide a detailed picture of heat transfer under different heating methods and material conditions, with the overarching aim of understanding how energy is distributed between the bed, the walls, and the gas phase. The analysis, therefore, relied on a comprehensive set of measurements to capture the thermal and radiative environment within the kiln. The temperatures of both the inner refractory wall and the outer shell were recorded to determine the magnitudes of local heat fluxes, while radiative intensity and the incident radiative wall heat flux were quantified with dedicated probes. In addition, flue gas temperatures and compositions were measured to evaluate gasphase compositions and enthalpy and to enable closure of the energy balance. Together, these measurements form the foundation for assessing how different heating methods and materials influence kiln performance. The complete set of measurements and their roles in the analysis are summarized in Table 4.

Table 4. Overview of the thermal and radiative measurements performed in Kiln Zero.

Quantity	Measurement		Purpose				
		method					
Inner wall temperature	IR	thermography	Estimation	of	the	internal	
	(kiln	ports)	temperature	enviro	nment		
Outer wall temperature	IR thermography		Determination of shell radiation and			liation and	
	(shel	ll surface)	convective losses				
Radiative heat flux	Ellipsoidal		Quantification of local wall heat				
	radiometer		flux relevant to bed heating				
	(kil	n ports)					
Radiative intensity	NAR (kiln		Characterization of axial variation			variation	
	ports)		in wall-directed radiation				
Flue gas temperature	Thermocouples		Flue gas ent	halpy	and en	nergy loss	
			estimation				
Flue gas composition	FTIR, HORIBA		Mass balance closure and flue ga			d flue gas	
$(\mathrm{CO}_2,\mathrm{O}_2,\mathrm{CO},\mathrm{N}_2)$			enthalpy				

The first clear observation from these measurements is the effect on the thermal behavior of the bed material. When raw meal was introduced into the kiln, the temperature distribution along the wall showed higher inner wall temperatures and lower outer wall temperatures than in the corresponding limestone cases, particularly around the mid-section in proximity to ports 2 and 3. These results indicate the formation of a coating layer on the inner wall, which effectively acts as an insulating barrier by retaining heat inside the kiln and reducing convective and radiative losses through the shell (Fig. 5). The radiative intensity measurements support this interpretation, showing elevated intensities for raw meal compared to limestone, consistent with greater retention of radiative energy inside the kiln volume. In contrast, the coarse and less-adhesive nature of limestone particles prevented the development of a similar layer, resulting in more direct heat losses through the refractory. The full temperature and radiative intensity profiles for both materials are presented in Papers I and II.

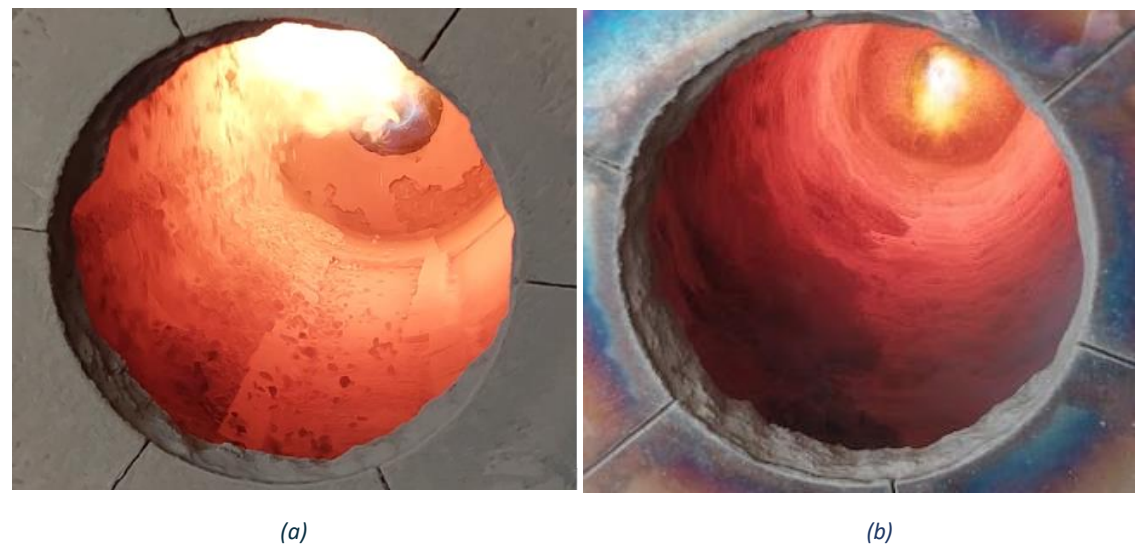


Figure 5 (a) Inner surface of the kiln operated with crushed limestone, where the lifters along the refractory wall are clearly visible and no coating layer is formed. (b) Inner surface of the kiln operated with fine raw meal, where the lifters are obscured by the buildup, indicating the formation of a continuous coating layer.

To evaluate the build-up layer formed by the raw meal, a rough experimental estimation of its thickness was performed by inserting a water-cooled metal rod through the kiln port and observing its alignment with the inner wall. This method suggested a coating thickness of between 5 cm and 7 cm. To complement this, a theoretical estimation was carried out using measured inner and outer wall temperatures, kiln geometry, and varying thermal conductivity values (k) typical of coating materials, by solving Equation (12) presented in the *Methods* section. The resulting thickness profiles along the kiln axis, as shown in Figure 6, demonstrated good agreement with the rod-based estimation for k-values in the range of 0.8–1.0 W/m·K. The build-up thickness peaked at ports 2 and 3 and decreased toward the kiln outlet, aligning with the highest inner wall temperatures and radiative intensities. This comparison validates the simplified estimation method and highlights the sensitivity of the coating layer to both material properties and local process conditions. Although coating formation was not the primary focus of the study, these findings provide important insights into its role in modifying kiln heat transfer behavior and underscore its relevance for practical kiln operation.

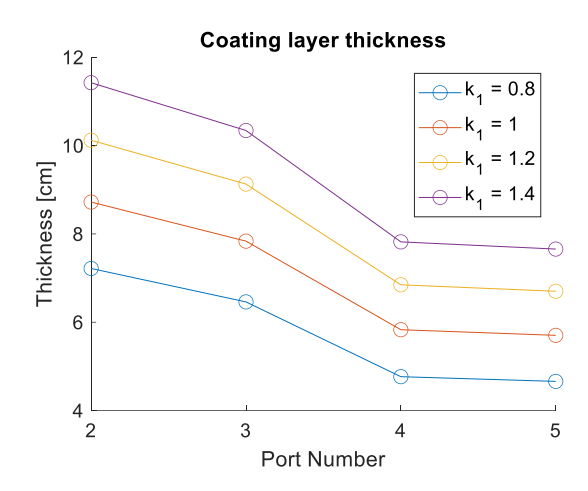
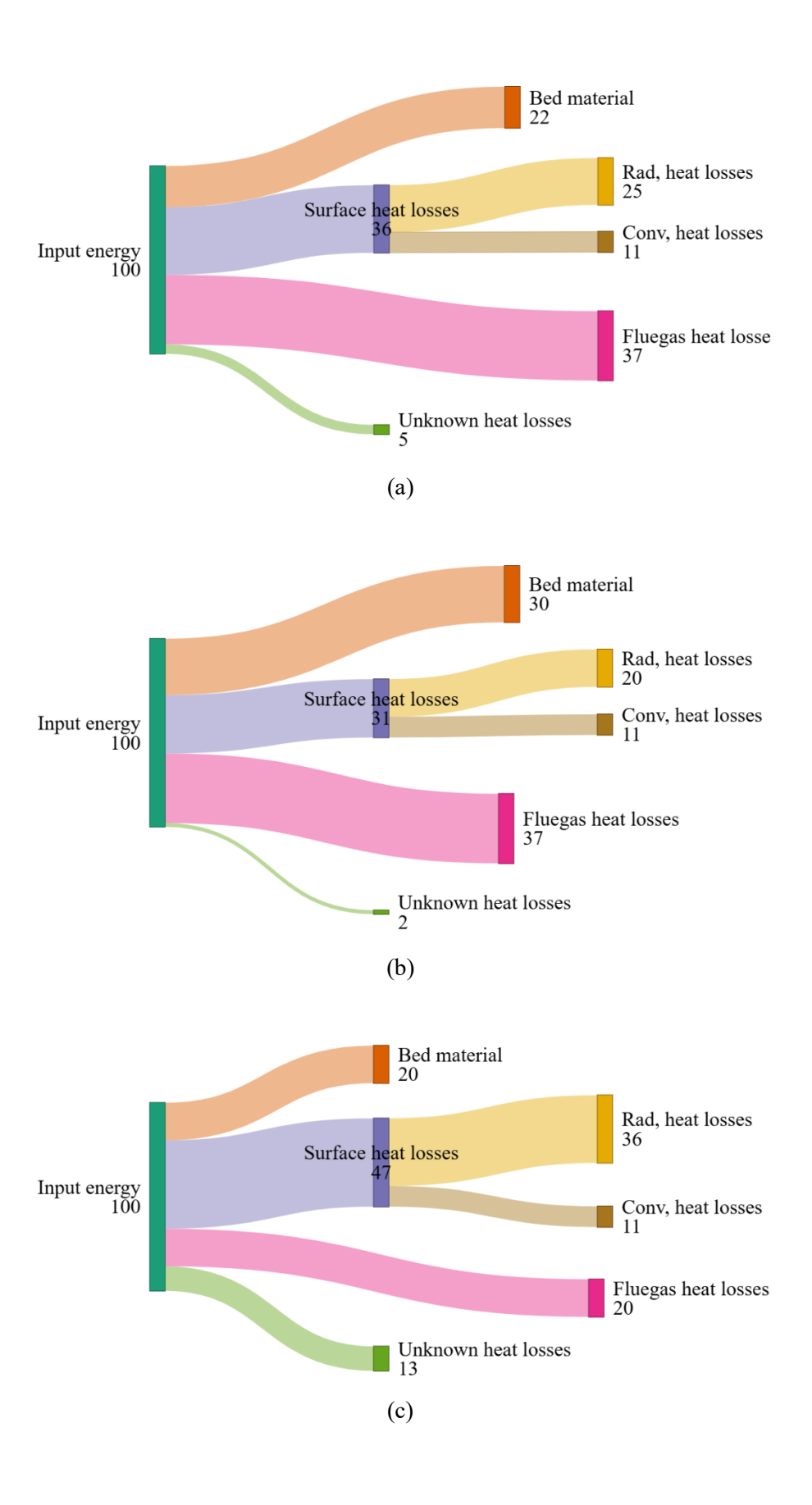


Figure 6: Variation of the build-up layer thickness along the different ports in the kiln, exhibiting the effect of material thermal conductivity on the coating layer.

With the influence of the coating layer established, the next step was to construct complete mass and energy balances for each heating configuration: propane combustion; oxygen-enriched propane combustion; and resistance heating. The balances required steady-state operation and integration of the measured inputs, which included the fuel flow rate, bed material feed, calcination degree, wall temperatures, radiative fluxes, and flue gas compositions. Mass balance closure enabled estimation of air leakage, which was found to be considerable in the propane combustion case and contributed to the high flue gas flow rate. In contrast, the oxygen-enriched case exhibited a lower level of leakage due to the elevated burner inlet pressures that resulted from the higher fuel and oxygen flow rates. Resistance heating, which is devoid of combustion, resulted in minimal flue gas generation, with CO2 from calcination as the sole contributor. The inner and outer wall temperatures used for radiative and convective loss estimations [Eqs. (9) and (10)], were measured using IR thermography. Detailed profiles of the temperatures and gas compositions for the tested cases are presented in Paper I. The energy balance results, presented in Figure 7, show clear distinctions between the heat loss mechanisms for the different heating methods. For resistance heating (Fig. 7d), an electrical input of approximately 140 kW was calculated from the current and voltage measurements, of which around 52% was lost through radiation and convection at the shell. This finding aligns with the earlier work of Jacob et al.³¹, who studied the same kiln configuration with electrical heating and reported comparable wall heat loss fractions. Both studies reflect the more-uniform outer wall temperature distribution created in the absence of combustion. In the oxygen-enriched combustion case (Fig. 7c), the wall losses were reduced to roughly 47%, although this advantage was offset by increased gas-phase losses associated with combustion products. Conventional propane combustion (Fig. 7, a and b) showed the poorest performance, with large contributions from both wall and flue gas losses, outcomes directly linked to leakage at the burner interface.



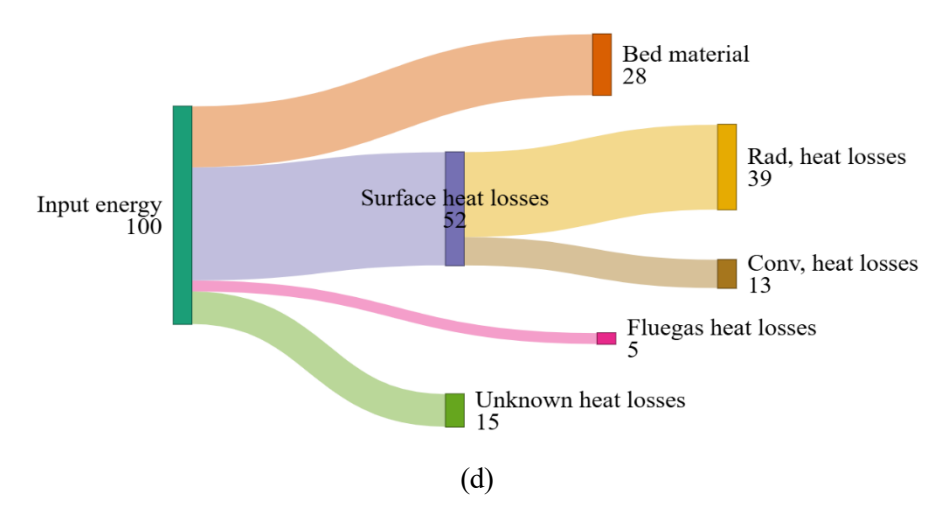


Figure 7: Sankey diagrams representing the energy balances of: (a) Limestone with conventional propane combustion (b) Raw meal conventional propane combustion; (c) Limestone with oxygenenriched combustion; (d)Limestone with Resistance heating elements. The numbers represent the percentages of total energy input

The closure of the energy balances was within 15% for all the cases, with the exception of resistance heating, for which larger deviations were observed. A sensitivity analysis confirmed that the flue gas and outer wall temperatures were the most-important variables affecting the loss estimations across all heating methods. The comparatively higher error for the oxygen-enriched case arose from uncertainty related to the supplied oxygen flow. For the electrified case, the assumption of negligible air ingress, combined with the dominance of shell radiation and convection in the output, introduced greater sensitivity to the outer wall temperature, contributing to the larger deviation. Taken together, these results highlight the decisive role of the heating method in determining how energy is partitioned between the walls, gases, and the bed, while also providing a robust foundation for scaling the analysis to industrial kilns.

Building on the experimental results obtained using Kiln Zero, a scaling analysis was performed to evaluate how heat transfer conditions and energy efficiency evolve in industrial-scale rotary kilns. By applying the same boundary conditions and heat loss methodology used at the 150-kW scale, the study assessed two industrial configurations: one for calcination based on the kiln described by Boateng (62.4 MW); and one for clinkerization based on the HMC kiln (116 MW). The analysis focused on three heating methods: conventional propane combustion, oxygen-enriched propane combustion, and resistance heating. The comparison revealed significant reductions in surface heat losses at an industrial scale due to a lower surface-to-volume ratio, especially for combustion-based systems. For instance, the surface losses dropped from 47% in the pilot kiln to 11% for scaled-up propane combustion and to 12% for oxygen-enriched propane. In contrast, resistance heating, which results in a more-uniform temperature distribution, showed relatively higher surface heat losses of 20%, despite scaling. Flue gas losses, on the other hand, were more sensitive to gas velocity and feed rates. These losses increased slightly for scaled-up propane combustion due to the higher gas velocities but decreased in the oxygen-

enriched case owing to higher combustion efficiency. For resistance heating, the flue gas losses remained low due to the absence of air leakage and combustion-related gases. Overall, the efficiency of energy transfer to the bed material improved at the industrial scale, with resistance heating reaching 60% efficiency compared to 45% for propane combustion. These findings highlight the importance of optimizing heating methods and kiln geometry during the scale-up process. A visual summary of the scaled energy distribution is presented in the Sankey diagrams in Figure 8. For the electrification case, the Sankey diagram includes an 8% share of "unknown losses", which represents the closure error of the balance rather than a physical loss pathway. This residual arises from the higher sensitivity of the electrified configuration to outer wall temperature, combined with the very small flue gas stream that is dominated by calcination CO₂. In contrast, the combustion cases are more tightly constrained by the fuel and stoichiometry, enabling near-complete closure of the balances at scale. Further numerical values and assumptions are detailed in Paper 1.

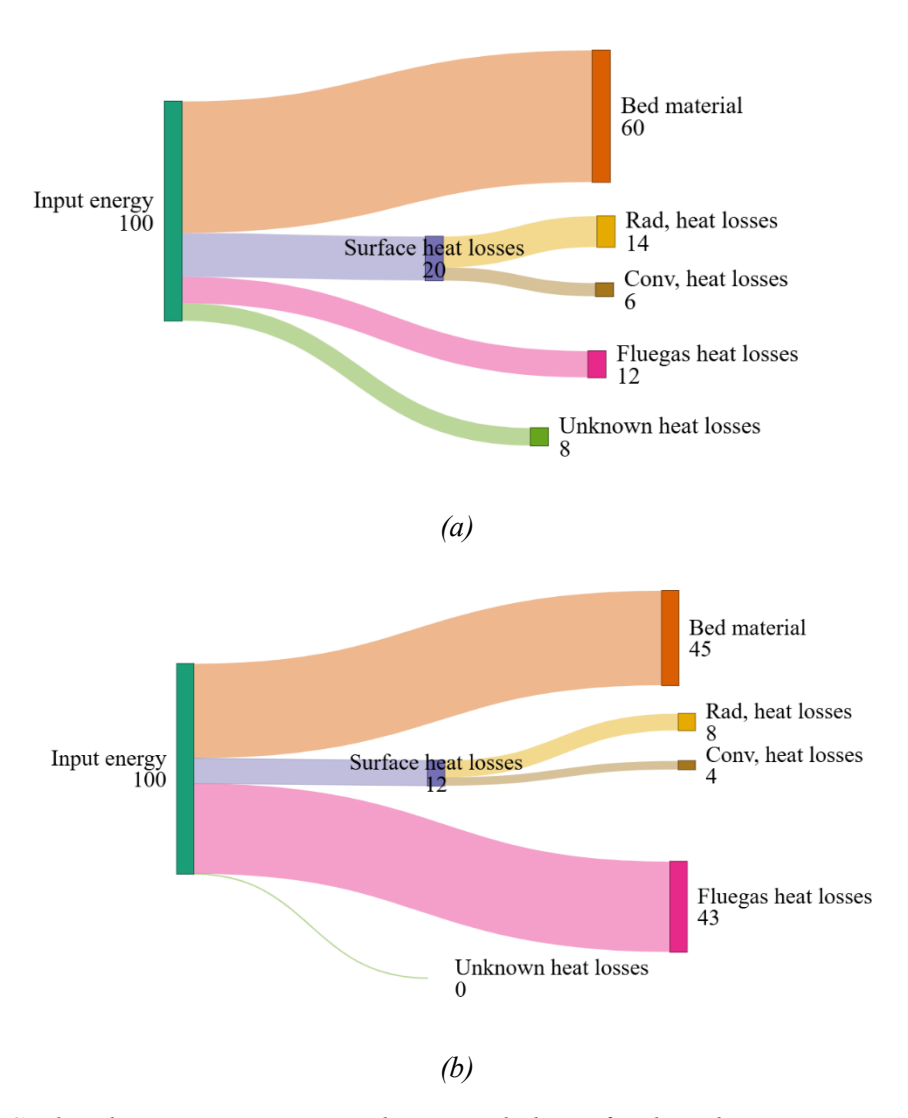


Figure 8: Sankey diagrams representing the energy balance for the calcination process using (a) electrification and (b) conventional combustion. The numbers represent the percentages of total energy input.

This study also presents a comparative analysis of the three heating technologies of conventional propane combustion, oxygen-enriched propane combustion, and resistance heating, which show distinct temperature distributions and energy loss pathways inside the kiln. Propane combustion exhibited high convective losses due to significant air leakage and flue gas generation, whereas oxygen-enriched combustion demonstrated improved thermal efficiency by reducing the flue gas volume and enhancing heat transfer to the bed material. Resistance heating produced a uniform axial temperature distribution, minimizing thermal gradients and ensuring stable heating conditions that were favorable for calcination. However, the absence of combustion gases led to a shift in energy losses, with higher surface heat losses dominating the energy balance. These thermal characteristics were supported by detailed measurements of the inner wall temperatures and radiative intensity profiles, which are presented and discussed in Paper 1.

In summary, the kiln experiments provide a comprehensive picture of the mechanisms governing heat transfer at pilot and industrial scales. The coating layer formed by the raw meal exerts a strong influence on wall losses and internal radiation, while the energy balances distinguish clearly between the loss structures of combustion-based and electrically heated kilns. Scaling to industrial conditions demonstrates how these mechanisms evolve with geometry, reducing the dominance of wall losses while shifting the balance of gas-phase losses according to combustion efficiency. Taken together, these results establish a detailed framework for understanding and comparing heating technologies in rotary kilns, and for evaluating their implications under industrially relevant conditions.

4.2 Experimental studies in the open air

Based on the results obtained from the heat transfer investigations inside the rotary kiln, an independent set of experiments was conducted in open-air conditions to study the characteristics of a CO₂-based thermal plasma plume before integrating it into the kiln. These experiments were designed to explore the radiative behaviors and spatial intensity distributions of the plasma under varying operational conditions, such as different arc currents and CO₂ flow rates. Unlike the kiln studies, this setup allowed for a direct line-of-sight assessment of plasma jet geometry and radiation characteristics in an unconfined environment. Thus, the open-air configuration offered an opportunity to isolate and analyze the behavior of the plasma plume itself, without the complexities introduced by the kiln walls, bed materials, or internal gas circulation.

Radiative intensity measurements provided direct insights into how thermal energy was distributed along the CO₂-based plasma plumes, as compared with a CH₄/O₂ combustion flame of similar effect (Fig. 9). The 50-kW_{el} plasma jet exhibited a gradual decline in intensity, from about 6.3 to 3.7 kW m⁻² sr⁻¹ for distances between 5 mm and 140 mm, reflecting plume expansion and mixing with ambient air, while the combustion flame showed a lower near-field intensity but had a longer luminous region, sustained by soot radiation (Fig. 9a). In contrast, the 300-kW_{el} plasma displayed a strongly localized

radiative peak that exceeded 100 kW m⁻² sr⁻¹ at 5 mm, followed by a sharp drop near 50 mm and partial recovery to 8–10 kW m⁻² sr⁻¹ beyond 100 mm. This abrupt decrease, supported by concurrent IR imaging (see Paper III), corresponded to the necking region, where radial contraction of the plume limited overlap with the narrow viewing cone of the radiometer. With an effective solid angle of ~9.5 × 10⁻⁵ sr, the measurements are highly sensitive to small geometric shifts of the emission core. The downstream recovery in intensity indicated continued emission and convective transport, despite reduced direct radiative coupling. The comparison of radiative intensity and calculated gas enthalpy further showed that maximum radiation did not scale linearly with total power input but rather depended upon the probe's alignment with the localized hotspot. These observations demonstrate that plasma jets exhibit concentrated radiative zones close to the outlet, transitioning toward convective dominance downstream, and they underline the importance of spatial resolution when characterizing the heat transfer behaviors of CO₂-based thermal plasmas. The statistical analysis of the results for the 300-kW_{el} cases is provided in the supporting information of Paper III.

Infrared (IR) imaging was used to visualize and to interpret qualitatively the geometries and stability levels of CO2-based plasma plumes across a broad range of operating conditions. Clear differences were observed between the 50-kWel and 300-kWel systems. The lower-power torch exhibited a diffuse, conical plume with gradual radial expansion, whereas the higher-power torch produced a moreelongated structure. The IR cameras operated with different presets. The 50-kWel images used a lowthreshold preset with longer integration and higher gain, yielding higher counts from cooler peripheral regions and an apparently longer plume. In contrast, the 300-kWel images used a high threshold preset with shorter integration and calibrated optical attenuation, yielding lower counts from cooler regions and emphasizing the hot core near the burner. Since the underlying count scales and effective cut-offs differ, apparent plume length and brightness are not directly comparable, so interpretation relies on the quantitative radiative measurements. A recurring feature in the 300-kWel cases was a localized radial constriction, referred to as 'necking', typically forming 60-70 mm downstream of the outlet. The minimum plume diameter decreased from about 14 mm at 200 A to roughly 6 mm at 300 A, and partially increased to ~9 mm when the CO₂ flow increased to 55 Nm³/h. This inverse relationship between current and neck width suggests electromagnetic pinch effects, whereby higher arc currents induce stronger azimuthal magnetic fields that compress the plasma column radially. While the present study does not provide a quantitative proof, this behavior is consistent with the Z-pinch constriction reported by Polukhin et al^{76,77}. Moreover, although aerodynamic effects cannot be completely excluded due to uncertainties related to the bulk plasma temperature, the observed trends support an electromagnetic origin. The opposing effect of increased flow rate indicates that gas dynamics mitigate this constriction by enhancing convective expansion and dilution The presence of necking also explains the sharp intensity drop observed in the NAR profiles at 50 mm; in this region, the contracted plume reduces overlap with the radiometer's narrow field of view, causing an apparent decrease in the recorded intensity even though the plasma remains highly emissive. Downstream of the necking zone, IR thermograms revealed an extended luminous region and strong glow from the tungsten rod reference, confirming the existence of persistent heating beyond the immediate radiative hotspot. Together with the axial intensity data, the IR observations establish a coherent picture of heat transfer within CO₂-based plasma jets, an intense, localized radiative core near the nozzle transitioning to convection-dominated energy transport downstream, governed by the coupled effects of current, flow, and magnetic confinement. A full set of thermographic images and parametric mapping of neck behavior is provided in Paper III.

The comparison of the plasma and combustion systems has important implications for process integration in enclosed reactors, such as rotary kilns. During plasma heating, the intense near-field radiation observed in the measurements would be further amplified by wall reflections, concentrating the heat fluxes around the burner region. This localized radiative load necessitates careful refractory selection, burner mounting, and potential shielding, so as to prevent material degradation near the inlet. Further downstream, however, the data show that convective transport becomes dominant as the radiative output decreases, which suggests that the plasma can sustain effective heat delivery along the kiln length through a hot gas flow. While combustion flames exhibit lower peak radiative intensity, they maintain a longer luminous zone that distributes radiation more evenly along the axis, leading to smoother temperature gradients. When confined within kiln walls, these fundamental differences in energy distribution will translate into distinct heat transfer behaviors, with plasma creating a concentrated radiative hotspot followed by convective propagation, and combustion providing diffuse, steady radiative heating. These insights, supported by the spatially resolved radiative intensity and IR imaging results, offer a physical basis for future numerical modeling and burner optimization.

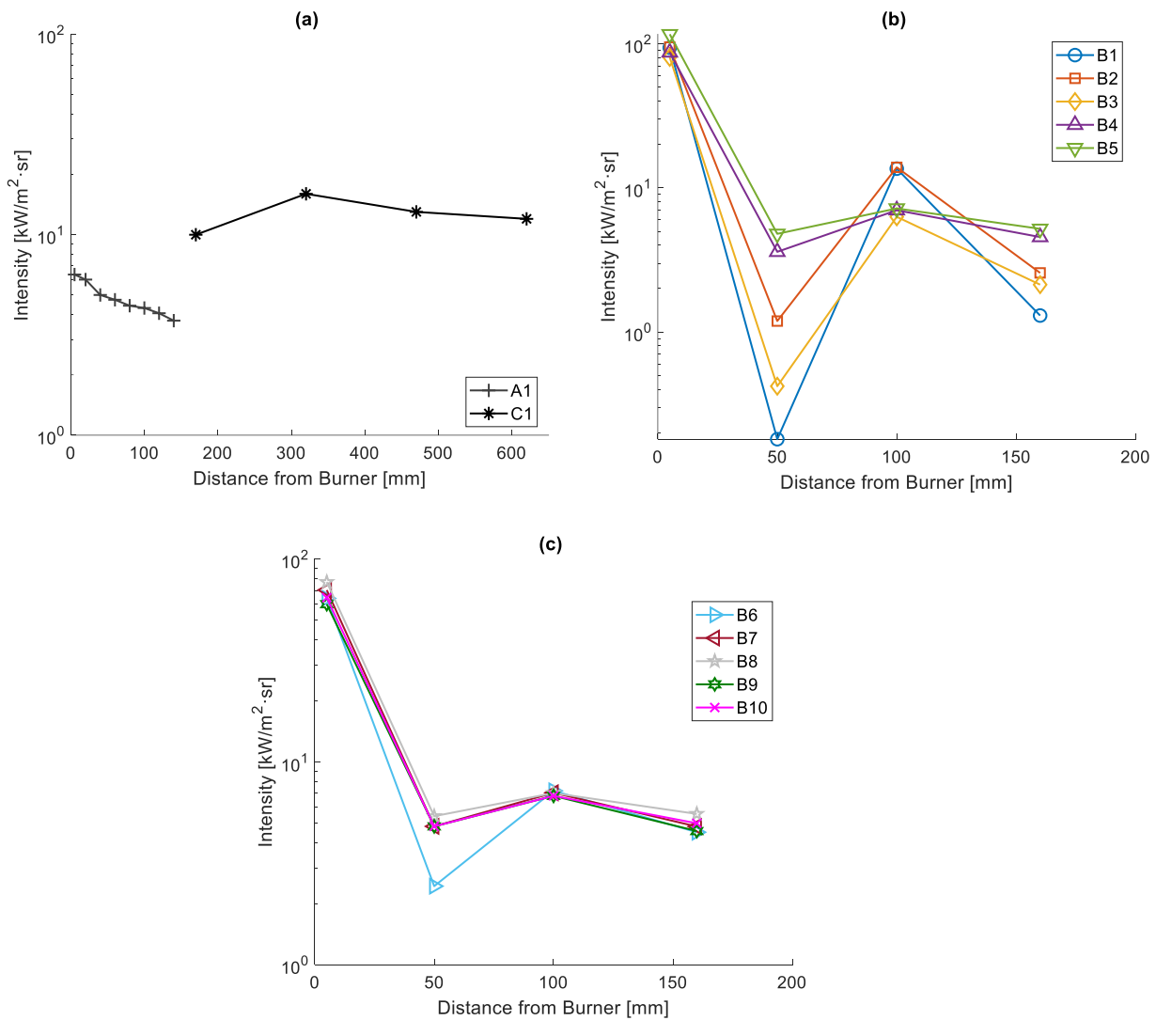


Figure 9 Axial radiative intensity measurements. (a) Comparison of the 50 kW_{el} plasma generator (A1) and the stoichiometric CH₄/O₂ combustion flame at 60 kW in open air (C1). The probe positions differ between the datasets due to the plume and flame length, with the comparison focusing on magnitude and trend. (b) Radiative intensity profiles for the 300 kW_{el} plasma generator cases (B1–B5) (c) Radiative intensity profiles for the 300 kW_{el} plasma generator cases (B6–B10).

5. Conclusion

This thesis has examined the heat transfer performances, energy efficiencies, and thermal behaviors associated with the use of different heating technologies in a rotary kiln, complemented by a detailed study of thermal plasma jets as a future electrification strategy. The work has addressed four research questions through three experimental studies. Paper I studied propane combustion, oxygen-enriched combustion, and resistance heating at pilot scale, including scaling analyses to industrial conditions. Paper II focused on the role of the bed material and coating layer formation inside the kiln using crushed raw meal as well as its impact on heat losses. Paper III characterized the radiative and geometrical behaviors of a CO₂-based thermal plasma jet under open-air conditions.

RQ1 – How do different heating technologies affect the overall heat transfer and energy balance in pilot rotary kilns?

The experimental results from the pilot kiln showed that each heating method exhibits distinct thermal characteristics. Propane-based combustion, used as a reference, showed increased flue gas losses due to air leakage and high gas volumes. In contrast, oxygen-enriched combustion achieved the lowest flue gas losses among the combustion cases due to minimal air leakage, along with the high temperatures needed for clinker formation. Resistance heating produced a uniform axial temperature profile, minimizing the thermal gradients and enhancing stability.

RQ2 – How do different bed materials influence wall heat losses in rotary kilns through coating layer formation?

Experiments using crushed raw meal revealed coating layer formation on the kiln wall, which served as a form of thermal insulation, stabilizing the wall temperatures, and reducing surface heat losses as compared to the use of limestone, for which no coating formation was observed. The thickness of the coating layer was estimated using measured wall temperatures and thermal conductivity assumptions, with the results aligning well with visual observations.

RQ3 – How do different heating technologies scale to industrial rotary kilns?

When scaled to industrial conditions, the combustion systems benefited from reduced surface heat losses due to a lower surface-to-volume ratio, while resistance heating retained low flue gas losses through improved thermal control. Oxygen enrichment enhanced thermal efficiency, whereas resistance heating offered the best energy utilization for electrified calcination.

RQ4 – Which of the radiative characteristics and heat transfer regime transitions of CO₂-based thermal plasma jets are relevant to kiln heating?

Measurements of CO₂ plasma plumes showed a localized near-field radiative hotspot close to the burner, followed by a steep intensity drop and subsequent stabilization downstream. This pattern, supported by

IR thermography, confirms a transition from intense localized radiation to downstream convective heat transport. These insights are crucial for future integration of plasma systems into rotary kilns, where localized radiative heating near the burner would be followed by convective energy transfer along the gas path.

Taken together, the findings of this thesis establish a foundation for understanding and optimizing heat transfer in rotary kilns under both combustion and electrified scenarios. The integration of coating dynamics, energy balance, and plasma heat transfer measurements provides a comprehensive experimental basis to support the transition toward more-efficient, flexible, and low-emissions thermal processing systems.

6. Future Work

The next phase of this research will focus on integrating CO₂-based plasma torches into rotary kilns under real-life process conditions. A series of campaigns has already been initiated using the same 150-kW rotary kiln, in which plasma is tested under varying power inputs, kiln speeds, and tilt angles, as well as with different bed materials (limestone and raw meal). These efforts will be expanded and analyzed in the forthcoming work for my PhD, in which I will assess material conversion, process stability, and heat transfer under electrified conditions.

In parallel, hybrid plasma systems, combining plasma with fuels such as hydrogen and methane, are being examined for application to glass melting. Open-air tests have been conducted to study plume behaviors, followed by pilot-scale trials in a glass furnace without batch charge. Upcoming work will include full-scale tests with a raw glass material, to evaluate the heating performance and melting behavior under hybrid plasma conditions.

To understand better the plasma-material interactions and to support model validation, advanced diagnostics will be incorporated into both the kiln and furnace tests. Spectroscopic measurements will be used to identify gas-phase species and to estimate local plasma temperatures. These measurements, combined with gas sampling, will provide insights into the dissociation pathways, reaction kinetics, and energy transfer mechanisms that occur in both pure and hybrid plasma systems. Notably, preliminary observations suggest that temperature readings obtained from different optical instruments, each with distinct spectral sensitivities, can diverge under identical plasma conditions. This highlights the complex nature of wall and gas-phase radiation interactions in plasma environments and underlines the need for careful selection and development of measurement strategies. Future work will, therefore, include a comparative study of diagnostic techniques, to establish reliable methods for temperature estimation and radiative heat transfer analysis in thermal and hybrid plasma systems. Together, these investigations will establish a robust experimental foundation for the development of predictive models and for scaling electrified heating technologies across energy-intensive industries.

References

- (1) Heidelberg Materials. *In line with Corporate Net Zero Standard: SBTi validates Heidelberg Materials' 2050 carbon reduction targets*. https://www.heidelbergmaterials.com/en/ir-2025-01-21 (accessed 2025-06-22).
- (2) Heidelberg Materials. *CemZero*. https://www.cement.heidelbergmaterials.se/sv/cemzero (accessed 2025-06-22).
- (3) Mastorakos, E.; Massias, A.; Tsakiroglou, C. D.; Goussis, D. A.; Burganos, V. N.; Payatakes, A. C. CFD Predictions for Cement Kilns Including Flame Modelling, Heat Transfer and Clinker Chemistry. *Appl Math Model* **1999**, *23* (1), 55–76. https://doi.org/10.1016/S0307-904X(98)10053-7.
- (4) Jonsson, C. Y. C.; Stjernberg, J.; Wiinikka, H.; Lindblom, B.; Boström, D.; Öhman, M. Deposit Formation in a Grate-Kiln Plant for Iron-Ore Pellet Production. Part 1: Characterization of Process Gas Particles. *Energy & Fuels* 2013, 27 (10), 6159–6170. https://doi.org/10.1021/ef400973w.
- (5) Mungyeko Bisulandu, B.-J. R.; Huchet, F. Rotary Kiln Process: An Overview of Physical Mechanisms, Models and Applications. *Appl Therm Eng* **2023**, *221*, 119637. https://doi.org/10.1016/j.applthermaleng.2022.119637.
- (6) Jarod Ryan. CFD Modelling of Heat Transfer and Calcination in Rotary Lime Kilns, University of Toronto, 2024.
- (7) Boateng, A. A. B. Rotary Kilns: Transport Phenomena and Transport Processes; 2006.
- (8) Zieri, W.; Ismail, I. Alternative Fuels from Waste Products in Cement Industry. In Handbook of Ecomaterials; Springer International Publishing: Cham, 2019; pp 1183– 1206. https://doi.org/10.1007/978-3-319-68255-6 142.
- (9) Nielsen, A. R. Combustion of Large Solid Fuels in Cement Rotary Kilns, Technical University of Denmark, 2012.
- (10) Carriço, A.; Bogas, J. A.; Guedes, M. Thermoactivated Cementitious Materials A Review. Constr Build Mater 2020, 250, 118873. https://doi.org/10.1016/j.conbuildmat.2020.118873.
- (11) Adrian Gunnarsson. Radiative Heat Transfer in Suspension-Fired Systems, Chalmers University of Technology, Gothenburg, 2019.
- (12) Tscheng, S. H.; Watkinson, A. P. Convective Heat Transfer in a Rotary Kiln. *Can J Chem Eng* **1979**, *57* (4), 433–443. https://doi.org/10.1002/cjce.5450570405.
- (13) Watkinson, A. P.; Brimacombe, J. K. Heat Transfer in a Direct-Fired Rotary Kiln: II. Heat Flow Results and Their Interpretation. *Metallurgical Transactions B* **1978**, *9* (2), 209–219. https://doi.org/10.1007/BF02653686.
- (14) Klas Andersson. Characterization of Oxy-Fuel Flames Their Composition, Temperature and Radiation, Chalmers, Gothenburg, 2007.

- (15) Gorog, J. P.; Adams, T. N.; Brimacombe, J. K. Regenerative Heat Transfer in Rotary Kilns. *Metallurgical Transactions B* **1982**, *13* (2), 153–163. https://doi.org/10.1007/BF02664572.
- (16) Eckert, E. R. G. Radiative Transfer, H. C. Hottel and A. F. Sarofim, McGraw-Hill Book Company, New York, 1967. 52 Pages. AIChE Journal 1969, 15 (5), 794–796. https://doi.org/10.1002/aic.690150504.
- (17) Howell, J. R.; Mengüç, M. P.; Daun, K.; Siegel, R. *Thermal Radiation Heat Transfer*; CRC Press: Seventh edition. | Boca Raton: CRC Press, 2021. | Revised edition of: Thermal radiation heat transfer / John R. Howell, M. Pinar Mengüç, Robert Siegel. Sixth edition. 2015., 2020. https://doi.org/10.1201/9780429327308.
- (18) Modest, M. F. *Radiative Heat Transfer*; Elsevier, 2013. https://doi.org/10.1016/C2010-0-65874-3.
- (19) Barr, P. V.; Brimacombe, J. K.; Watkinson, A. P. A Heat-Transfer Model for the Rotary Kiln: Part II. Development of the Cross-Section Model. *Metallurgical Transactions B* **1989**, *20* (3), 403–419. https://doi.org/10.1007/BF02696992.
- (20) Mujumdar, K. S.; Ranade, V. V. Simulation of Rotary Cement Kilns Using a One-Dimensional Model. *Chemical Engineering Research and Design* 2006, 84 (3 A), 165– 177. https://doi.org/10.1205/cherd.04193.
- (21) Singh, A. P.; Ghoshdastidar, P. S. Computer Simulation of Heat Transfer in Alumina and Cement Rotary Kilns. *J Therm Sci Eng Appl* **2022**, *14* (3). https://doi.org/10.1115/1.4051376.
- (22) Spang, H. A. A Dynamic Model of a Cement Kiln. *Automatica* **1972**, *8* (3), 309–323. https://doi.org/10.1016/0005-1098(72)90050-7.
- (23) Guruz, H. K.; Bac, N. Mathematical Modelling of Rotary Cement Kilns by the Zone Method. *Can J Chem Eng* **1981**, *59* (4), 540–548. https://doi.org/10.1002/cjce.5450590423.
- (24) Mastorakos, E.; Massias, A.; Tsakiroglou, C. D.; Goussis, D. A.; Burganos, V. N.; Payatakes, A. C. CFD Predictions for Cement Kilns Including Flame Modelling, Heat Transfer and Clinker Chemistry. *Appl Math Model* **1999**, *23* (1), 55–76. https://doi.org/10.1016/S0307-904X(98)10053-7.
- (25) Agrawal, A.; Ghoshdastidar, P. S. Computer Simulation of Heat Transfer in a Rotary Lime Kiln. *J Therm Sci Eng Appl* **2018**, *10* (3). https://doi.org/10.1115/1.4039299.
- (26) A. A. Boateng. Rotary Kiln Transport Phenomena: A Study of the Bed Motion and Heat Transfer, University of British Columbia, 1993. https://doi.org/10.14288/1.0078512.
- (27) Henein, H.; Brimacombe, J. K.; Watkinson, A. P. Experimental Study of Transverse Bed Motion in Rotary Kilns. *Metallurgical Transactions B* **1983**, *14* (2), 191–205. https://doi.org/10.1007/BF02661016.
- (28) Liu, X. Y.; Specht, E. Temperature Distribution within the Moving Bed of Rotary Kilns: Measurement and Analysis. *Chemical Engineering and Processing: Process Intensification* **2010**, *49* (2), 147–150. https://doi.org/10.1016/j.cep.2010.01.008.

- (29) Watkinson, A. P.; Brimacombe, J. K. Limestone Calcination in a Rotary Kiln. *Metallurgical Transactions B* **1982**, *13* (3), 369–378. https://doi.org/10.1007/BF02667752.
- (30) Butler, B. W.; Denison, M. K.; Webb, B. W. Radiation Heat Transfer in a Laboratory-Scale, Pulverized Coal-Fired Reactor. *Exp Therm Fluid Sci* **1994**, *9* (1), 69–79. https://doi.org/10.1016/0894-1777(94)90010-8.
- (31) Jacob, R. M.; Tokheim, L.-A. Novel Design of a Rotary Calciner Internally Heated with Electrical Axial Heaters: Experiments and Modelling. *Results in Engineering* **2023**, *17*, 100992. https://doi.org/10.1016/j.rineng.2023.100992.
- (32) Engin, T.; Ari, V. Energy Auditing and Recovery for Dry Type Cement Rotary Kiln Systems A Case Study. *Energy Convers Manag* **2005**, *46* (4), 551–562. https://doi.org/10.1016/j.enconman.2004.04.007.
- (33) Söğüt, Z.; Oktay, Z.; Karakoç, H. Mathematical Modeling of Heat Recovery from a Rotary Kiln. *Appl Therm Eng* **2010**, *30* (8–9), 817–825. https://doi.org/10.1016/j.applthermaleng.2009.12.009.
- (34) Ustaoglu, A.; Alptekin, M.; Akay, M. E. Thermal and Exergetic Approach to Wet Type Rotary Kiln Process and Evaluation of Waste Heat Powered ORC (Organic Rankine Cycle). Appl Therm Eng 2017, 112, 281–295. https://doi.org/10.1016/j.applthermaleng.2016.10.053.
- (35) Sahoo, N.; Kumar, A.; Samsher. Review on Energy Conservation and Emission Reduction Approaches for Cement Industry. *Environ Dev* **2022**, *44*, 100767. https://doi.org/10.1016/j.envdev.2022.100767.
- (36) Acharya, P.; Fogo, D.; McBride, C. Process Challenges in Rotary Kiln-based Incinerators in Soil Remediation Projects. *Environmental Progress* **1996**, *15* (4), 267–276. https://doi.org/10.1002/ep.670150417.
- (37) Shahin, H.; Hassanpour, S.; Saboonchi, A. Thermal Energy Analysis of a Lime Production Process: Rotary Kiln, Preheater and Cooler. *Energy Convers Manag* **2016**, *114*, 110–121. https://doi.org/10.1016/j.enconman.2016.02.017.
- (38) Tran, H. N.; Barham, D. An Overview of Ring Formation in Lime Kilns Mud Rings, Mid-Kiln Rings, and Front-End Rings Form at Different Locations in The.
- (39) Ravindran, J.; Krishnan, S. Studies on Thermal Analysis of Cement Rotary Kiln Based on Clinker Coating Materials on Refractories, Energy and Monetary Savings. *Congress on Recent Development in Engineering and Technology (RDET-16)*. **2016**.
- (40) Akbari, K., Ghayebloo, A., Yousefi, M. R. Identification of Coating Thickness in Cement Rotary Kiln. *Iranian Journal of Chemistry and Chemical Engineering* **2022**, *41*, 1746–1754.
- (41) Wirtz, S.; Pieper, C, Buss, F, Schiemann, M., Schaefer, S., & Scherer, V. Impact of Coating Layers in Rotary Cement Kilns: Numerical Investigation with a Blocked-off Region Approach for Radiation and Momentum. *Thermal Science and Engineering Progress* **2020**, *15*.

- (42) DANIEL BÄCKSTRÖM. Experimental and Modelling Studies of Particle Radiation in Flames, CHALMERS UNIVERSITY OF TECHNOLOGY, Gothenburg, 2015.
- (43) ELIAS EHLMÉ. Radiative Transfer Models for Rotary Kilns from Fossil Fuels to Hydrogen Gas and Thermal Plasmas, CHALMERS UNIVERSITY OF TECHNOLOGY, Gothenburg, 2025.
- (44) Fakt, A.; Gunnarsson, A.; Andersson, K.; Normann, F.; Wilhelmsson, B. Evaluating Heat Transfer Conditions in a Plasma-Heated Rotary Kiln for Cement Production. *Ind Eng Chem Res* **2025**, *64* (16), 8329–8338. https://doi.org/10.1021/acs.iecr.5c00220.
- (45) Boulos, M. I.; Fauchais, P.; Pfender, E. *Thermal Plasmas: Fundamentals and applications: Volume 1.*; Springer US: Boston, MA, 1994. https://doi.org/10.1007/978-1-4899-1337-1.
- (46) Bogaerts, A.; Centi, G. Plasma Technology for CO2 Conversion: A Personal Perspective on Prospects and Gaps. *Front Energy Res* **2020**, *8*. https://doi.org/10.3389/fenrg.2020.00111.
- (47) Amarnath, P.; Nandy, N.; Indumathy, B.; Yugeswaran, S. Study on CO2 Based Thermal Plasma Torch and Its Effective Utilization for Material Processing in Atmospheric Pressure. *Journal of CO2 Utilization* **2022**, *66*, 102290. https://doi.org/10.1016/j.jcou.2022.102290.
- (48) Samal, S. Thermal Plasma Technology: The Prospective Future in Material Processing. *J Clean Prod* **2017**, *142*, 3131–3150. https://doi.org/10.1016/j.jclepro.2016.10.154.
- (49) Lu, Q.; Lei, W.; Yue, W.; Huang, W.; Dong, Y.; Yan, W.; Liu, Y.; Chen, Y.; Zhao, Y. Reaction Mechanism Explorations on Non-Thermal Plasma Reforming of CO2-CH4 by Combining Kinetics Modeling and Emission Spectroscopy Measurements. *Fuel* **2023**, *344*, 128041. https://doi.org/10.1016/j.fuel.2023.128041.
- (50) George, A.; Shen, B.; Craven, M.; Wang, Y.; Kang, D.; Wu, C.; Tu, X. A Review of Non-Thermal Plasma Technology: A Novel Solution for CO2 Conversion and Utilization. *Renewable and Sustainable Energy Reviews* **2021**, *135*, 109702. https://doi.org/10.1016/j.rser.2020.109702.
- (51) Vadikkeettil, Y.; Amarnath, P.; Yugeswaran, S.; Ananthapadmanabhan, P. V. Comparative Study of Plasma Torch Characteristics Using Air and Carbon Dioxide. *IEEE Transactions on Plasma Science* 2022, 50 (6), 1395–1400. https://doi.org/10.1109/TPS.2021.3129593.
- (52) Fauchais, P.; Vardelle, A. Thermal Plasmas. *IEEE Transactions on Plasma Science* **1997**, *25* (6), 1258–1280. https://doi.org/10.1109/27.650901.
- (53) Taylor, P. R.; Pirzada, S. A. Thermal Plasma Processing of Materials: A Review. *Advanced Performance Materials* **1994**, *I* (1), 35–50. https://doi.org/10.1007/BF00705312.
- (54) Baskoro, A. S.; Supriadi, S.; Dharmanto. Review on Plasma Atomizer Technology for Metal Powder. MATEC Web of Conferences 2019, 269, 05004. https://doi.org/10.1051/matecconf/201926905004.

- (55) Jonkers, J.; Sande, M. van de; Sola, A.; Gamero, A.; Mullen, J. van der. On the Differences between Ionizing Helium and Argon Plasmas at Atmospheric Pressure. *Plasma Sources Sci Technol* **2003**, *12* (1), 30–38. https://doi.org/10.1088/0963-0252/12/1/304.
- (56) Bodil Wilhelmsson; Claes Kollberg; Johan Larsson; Jan Eriksson; Magnus Eriksson. Cemzero - a Feasibility Study Evaluating Ways to Reach Sustainable Cement Production via the Use of Electricity; Stockholm, 2018.
- (57) Wang, F.; Liu, H.; Liu, X.; Zhang, L.; Yang, P.; Zhang, T.; Yu, Z.; Li, H.; Cressault, Y. Calculation of Radiative Properties for [82%Ar-18%CO2]-Fe Plasmas in MAG Welding Arc. *Materials* **2022**, *15* (18), 6415. https://doi.org/10.3390/ma15186415.
- (58) El Khalloufi, M.; Soucy, G.; Lapointe, J.; Paquet, M. Reduction of an Ilmenite Concentrate by Using a Novel CO2/CH4 Thermal Plasma Torch. *Minerals* **2024**, *14* (5), 502. https://doi.org/10.3390/min14050502.
- (59) Zhukov, M.; Zasypkin, I. *Thermal Plasma Torches: Design, Characteristics, Application*; Cambridge Int Science Publishing, 2007.
- (60) Bonizzoni, G.; Vassallo, E. Plasma Physics and Technology; Industrial Applications. *Vacuum* **2002**, *64* (3–4), 327–336. https://doi.org/10.1016/S0042-207X(01)00341-4.
- (61) Gleizes, A.; Gonzalez, J. J.; Freton, P. Thermal Plasma Modelling. *J Phys D Appl Phys* **2005**, *38* (9), R153–R183. https://doi.org/10.1088/0022-3727/38/9/R01.
- (62) Murphy, A. B.; Park, H. Modeling of Thermal Plasma Processes: The Importance of Two-Way Plasma-Surface Interactions. *Plasma Processes and Polymers* 2017, 14 (1– 2). https://doi.org/10.1002/ppap.201600177.
- (63) Ko, J.; Kim, T.-H.; Choi, S. Numerical Simulation of Cement Kiln Combined with Thermal Plasma for SF ₆ Pyrolysis. *Applied Science and Convergence Technology* **2019**, *28* (4), 93–100. https://doi.org/10.5757/ASCT.2019.28.4.93.
- (64) Villarreal-Medina, R.; Murphy, A. B.; Méndez, P. F.; Ramírez-Argáez, M. A. Heat Transfer Mechanisms in Arcs of Various Gases at Atmospheric Pressure. *Plasma Chemistry and Plasma Processing* 2023, 43 (4), 787–803. https://doi.org/10.1007/s11090-023-10328-9.
- (65) Zhou, Y.; Zhu, L.; Yang, B.; Fan, L.; Meng, X.; Chu, R.; Jiang, X.; Li, P.; Li, W.; Chen, H. Heavy Metal Migration Regimes in the Production of Syngas from Solid Waste by Thermal Plasma Treatment. *J Hazard Mater* 2024, 461, 132698. https://doi.org/10.1016/j.jhazmat.2023.132698.
- (66) Zhang, Z.; Gou, Q.; Zhang, T.; Lu, X.; Xu, L.; Zhang, J. Simulation and Analysis of the Heat Transfer Mechanism of Arc Plasma with CMT plus Pulse Composite Heat Source. Welding in the World 2024, 68 (3), 525–541. https://doi.org/10.1007/s40194-023-01594-4.
- (67) Yugeswaran, S.; Selvarajan, V. Electron Number Density Measurement on a DC Argon Plasma Jet by Stark Broadening of Ar I Spectral Line. *Vacuum* **2006**, *81* (3), 347–352. https://doi.org/10.1016/j.vacuum.2006.06.001.

- (68) Hrabovsky, M.; Konrad, M.; Hlina, M.; Kopecky, V.; Kavka, T.; Chumak, O.; Maslani, A.; Van Oost, G. Plasma Aided Gasification of Biomass and Plastics Using CO2 as Oxidizer. *International Symposium on Non-Thermal/Thermal Plasma Pollution Control Technology & Sustainable Energy* **2010**, No. 7.
- (69) Wang, C.; Zhang, Z.; Cui, H.; Xia, W.; Xia, W. Characteristics of Helium DC Plasma Jets at Atmospheric Pressure with Multiple Cathodes. *Chinese Physics B* **2017**, *26* (8), 085207. https://doi.org/10.1088/1674-1056/26/8/085207.
- (70) YANG, T.; SHEN, J.; RAN, T.; LI, J.; CHEN, P.; YIN, Y. Understanding CO ₂ Decomposition by Thermal Plasma with Supersonic Expansion Quench. *Plasma Science and Technology* **2018**, *20* (6), 065502. https://doi.org/10.1088/2058-6272/aaa969.
- (71) Rida Galaly, A.; Van Oost, G.; Dawood, N. Sustainable Plasma Gasification Treatment of Plastic Waste: Evaluating Environmental, Economic, and Strategic Dimensions. *ACS Omega* **2024**, *9* (19), 21174–21186. https://doi.org/10.1021/acsomega.4c01084.
- (72) Karim Badr. Smelting of Iron Oxides Using Hydrogen Based Plasmas, Montanuniversität Leoben, Leoben, 2007.
- (73) Zarl, M. A.; Farkas, M. A.; Schenk, J. A Study on the Stability Fields of Arc Plasma in the HPSR Process. *Metals (Basel)* **2020**, *10* (10), 1394. https://doi.org/10.3390/met10101394.
- (74) Ernst, D.; Zarl, M. A.; Cejka, J.; Schenk, J. A New Methodological Approach on the Characterization of Optimal Charging Rates at the Hydrogen Plasma Smelting Reduction Process Part 2: Results. *Materials* **2022**, *15* (12), 4065. https://doi.org/10.3390/ma15124065.
- (75) Pauna, H.; Ernst, D.; Zarl, M.; Souza Filho, I. R. de; Kulse, M.; Büyükuslu, Ö.; Jovičević-Klug, M.; Springer, H.; Huttula, M.; Schenk, J.; Fabritius, T.; Raabe, D. The Optical Spectra of Hydrogen Plasma Smelting Reduction of Iron Ore: Application and Requirements. *Steel Res Int* **2024**, *95* (8). https://doi.org/10.1002/srin.202400028.
- (76) Polukhin, S. N.; Gurei, A. E.; Nikulin, V. Ya.; Peregudova, E. N.; Silin, P. V. Studying How Plasma Jets Are Generated in a Plasma Focus. *Plasma Physics Reports* **2020**, *46* (2), 127–137. https://doi.org/10.1134/S1063780X20020087.
- (77) Polukhin, S. N.; Nikulin, V. Ya.; Silin, P. V. On the Generation of Plasma Jets in the Kilojoule Plasma Focus Device. *Plasma Physics Reports* **2022**, *48* (4), 346–354. https://doi.org/10.1134/S1063780X22040110.
- (78) Auluck, S.; Kubes, P.; Paduch, M.; Sadowski, M. J.; Krauz, V. I.; Lee, S.; Soto, L.; Scholz, M.; Miklaszewski, R.; Schmidt, H.; Blagoev, A.; Samuelli, M.; Seng, Y. S.; Springham, S. V.; Talebitaher, A.; Pavez, C.; Akel, M.; Yap, S. L.; Verma, R.; Kolacek, K.; Keat, P. L. C.; Rawat, R. S.; Abdou, A.; Zhang, G.; Laas, T. Update on the Scientific Status of the Plasma Focus. *Plasma* **2021**, *4* (3), 450–669. https://doi.org/10.3390/plasma4030033.
- (79) Andersson, K.; Johansson, R.; Hjärtstam, S.; Johnsson, F.;; Leckner, B. Radiation Intensity of Lignite-Fired Oxy-Fuel Flames. *Exp. Therm. Fluid Sci.*, **2008**, *33*, 67–76.

(80) Andersson, K.; Johansson, R.; Johnsson, F.; Leckner, B. Radiation Intensity of Propane-Fired Oxy-Fuel Flames: Implications for Soot Formation. *Energy Fuels*, 22 (3), 1535–1541. **2008**, 22, 1535–1541.